

---

---

# **Finite element modeling of laser welding induced distortion due to initial residual stresses**

---

---

Master thesis

Aalborg University  
The Faculty of Engineering and Science



**AALBORG UNIVERSITY**  
STUDENT REPORT

**Title:**

**Semester:** 4<sup>th</sup> semester

**Project:** Master thesis

**ECTS:** 30

**Project period:** Spring semester 2020

**Main supervisor:** Benny Endelt

**Participants:**

*Elisabeth H. Ophaug*

---

Elisabeth Hasz  
Ophaug

eophau18@student.aau.dk

**Pages:** 42

**Appendix pages:** 5 pages

**Submitted:** June 2, 2020

**Faculty of-**  
**Engineering and Science**  
Manufacturing Engineering  
Fibigerstræde 16  
9220 Aalborg Øst  
<http://www.m-tech.aau.dk/>

**Abstract:**

Numerical simulation technology have in recent years developed and become widely used for welding simulation, to predict welding temperature field, residual stresses, distortion and optimization. However, the influence of initial stresses in the structure, prior to welding, have barely been investigated experimentally and numerically. In the present work, a computational approach based on thermal elastic plastic finite element method have been developed to clarify the effect of initial stresses on distortion in the welded structure. External load is applied, deforming the material in the plastic area and inducing the initial stresses prior to the laser welding process. After deformation, laser beam welding is conducted to joint the plates together. Through comparing the distortion in a structure after deformation induced stresses and welding with a structure without initial stresses after welding, the influence of initial residual stresses have been investigated. The numerical results show that the initial stresses have little to no effect on the distortion post welding.

# CONTENTS

<b>Preface</b>	<b>v</b>
<b>1 Introduction</b>	<b>1</b>
1.1 Background and motivation . . . . .	1
1.2 Project description . . . . .	2
1.2.1 Scope and objectives . . . . .	2
1.2.2 Design and material . . . . .	2
1.2.3 Case studies . . . . .	3
1.2.4 Stress Generating . . . . .	3
<b>2 Literature review</b>	<b>5</b>
<b>3 Finite Element Modeling</b>	<b>9</b>
3.1 Assumptions and exclusions . . . . .	10
3.2 Thermal conduction model . . . . .	10
3.3 Heat source model . . . . .	10
3.3.1 Laser welding and heat source parameters . . . . .	12
3.4 Thermal boundary conditions . . . . .	14
3.5 Material model . . . . .	16
3.6 Numerical model . . . . .	18
3.6.1 Elements . . . . .	18
3.6.2 Discretization . . . . .	18
3.6.3 Implicit . . . . .	20
3.6.4 Time step . . . . .	20
3.6.5 Weld . . . . .	21
3.6.6 Model boundary conditions . . . . .	22
<b>4 Results and discussion</b>	<b>23</b>
4.1 Goldak double ellipsoidal heat source . . . . .	23
4.1.1 Case A1 and A2 . . . . .	23
4.2 Conical heat source . . . . .	30
4.2.1 Case A1 and A2 . . . . .	30
4.3 Element distortion . . . . .	33
4.4 Summary . . . . .	33
4.5 Gap Closing . . . . .	34
4.6 Validation . . . . .	35

<b>5 Conclusion</b>	<b>37</b>
5.1 Further work . . . . .	37
<b>Bibliography</b>	<b>39</b>
<b>A Keyword deck</b>	<b>43</b>
A.1 Control keywords . . . . .	43
A.2 Database . . . . .	44
A.3 Implicit . . . . .	44
A.4 Boundary Conditions . . . . .	45
A.5 Parts and Material . . . . .	46
A.6 contact . . . . .	47

# PREFACE

This report is composed a student from 4th. semester on the education for Manufacturing Engineering at Aalborg University. A thank you goes to Benny Endelt and Anders Noel Thomsen for their support and guidance.

## Reading guide

- The report can be read independently of the appendices, that are meant as additional reading for further information.
- All source references are compiled in a bibliography at the back of the report.
- Figures, equations and charts are numbered according to chapter number, (i.e. 7.1 is the first figure in Chap 7. etc ). Appendices are indexed with capital letters.
- Nomenclature for various equations and formulas will be stated immediately under the equation or in the referring text, once established the same nomenclature is used trough the report.
- If not stated explicitly otherwise, units are assumed to be SI-units. Decimal point (.), is used as decimal separator.



# INTRODUCTION

## 1.1 Background and motivation

Laser beam welding is a welding technique in fast rising within manufacturing processes in numerous industries. The advantages of this welding technique includes high energy density and low heat input, compared to conventional welding techniques. Laser welding allows for higher welding speed, thus higher trough put rate, no additional material is needed during the process and it is a non-contact joining process.

Due to the high power density in the welding technique, it is possible to focus the laser beam power to a very small spot diameter. As a result the heat affected zone is smaller, lower distortion, residual stresses and strains, compared to conventional welding processes [1].

However, it is not possible to avoid residual stresses and distortion altogether, in the laser welding process. The local heating and subsequent non-uniform cooling of the material, will induce a complex distribution of stresses in the weld region and cause unwanted geometric distortions in the welded structure. As the welding induced distortion can make the assembling process problematic and also severely impair the performance and reliability of the welded structure, they must be properly dealt with.

Most welding processes operate in conduction mode, where the heat input from the laser light on the material surface is transferred through the material by conduction. In laser welding, where the power density usually is higher, the formation of a keyhole is present, accompanied by the phase change phenomena melting and evaporation. Due to the complex physical phenomena occurring in a very short time during the welding process, the optimization of the process is a difficult task. Conducting welding experimental based on trial and error are time consuming and with many operative difficulties increasing the total cost of the process [1].

A numerical approach to model the laser welding process have proven its importance by providing a deeper understand of the laser welding physics, making

it more reliable and relevant to industry applications. The process parameters of the laser welding process can be defined efficient to save time and cost.

The laser welding process is commonly one of several operations during the manufacturing of a structure. The part might undergo thermal or mechanical processes during the manufacturing process, prior to welding, which produce residual stresses due to local plastic deformation. These residual stresses have been found to in general have a negative impact on a structure. Their effect on the weld, specifically distortion, when present prior to welding should be investigated. Knowledge of the correlation between initial stresses and welding induced distortion would be beneficial as precautions could be made during design and manufacturing stage of the welded structure.

## 1.2 Project description

### 1.2.1 Scope and objectives

In this study, numerical simulation method based on finite element method and thermal conduction heat transfer is used to clarify the influence of initial residual stresses on distortion induced by welding in an austenitic stainless steel model. In the finite element model, a three point bending process is assumed to generate the initial residual stresses and a laser beam is used to perform the welding.

### 1.2.2 Design and material

Figure 1.1 illustrates the model of the structure used in this study. The structure consists of two parts, the rectangle plate, called the stiffener, has a length of 80 mm and a width of 60mm, and the bent plate has a height of 10 mm and a length of 100 mm. The material used for this purpose is EN-1.4301 stainless steel sheets with a thickness of 1.5 mm for both parts of the structure.

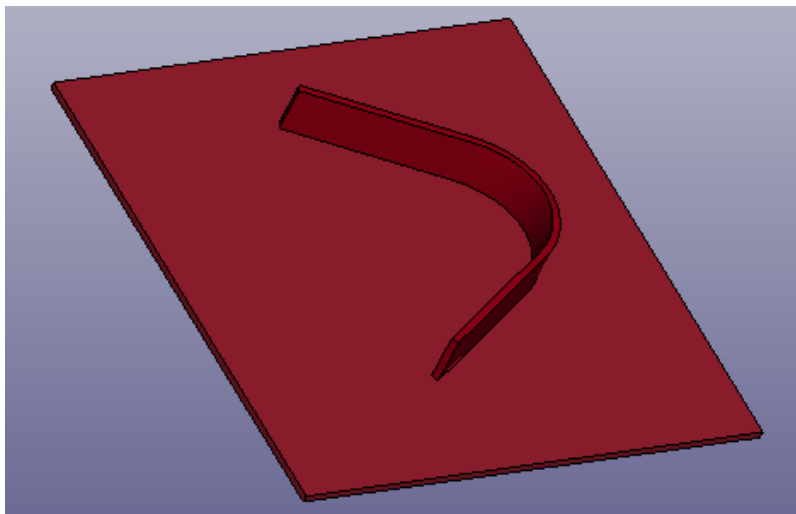


**Figure 1.1:** The configuration of the model used for the welding simulation.

Austenitic stainless steel EN-1.4301 is used in numerous industries due to having the advantages of low thermal conductivity, being a superior laser light absorber, high resistance to corrosion and high stability at elevated temperatures [2]. The composition as percentage of weight for standard stainless steel EN-1.4301 are presented in table 1.1 [3].

Elements	C	Si	Mn	N	Mo	Ni	Cr	Ti &Nb
wt %	0.02-0.08	0.50-3.00	1.00-2.00	0.00-0.15	0.00-2.00	19.00-20.00	16.00-25.00	0.00-0.20

**Table 1.1:** The chemical composition of standard stainless steel EN-1.4301.

### 1.2.3 Case studies

Two main case studies, A and B, were considered for the investigation to account for the stresses induced prior to the welding process. These two specimens will have the same geometry and material properties.

The intention is to ahead of the laser welding process have one structure with stresses and one with out, case A and B respectively, for comparison following the welding process. By having the models identical to each other, except for the initial stresses, any uncertainties surrounding other factors influencing the final distortion in the structure are removed.

Case A and B will both additionally have two different weld paths. A1 and B1 will be welded along the inside of the bent shape, and A2 and B2 will be welded along the outer line. This has the objective of deciding if the placement of the weld seam will influence distortion in the structure.

- Case A1: Initial stresses and welded along the inner line of the bent shape.
- Case A2: No initial stresses and welded along the inner line of the bent shape.
- Case B1: Initial stresses and welded along the outer line of the bent shape.
- Case B2: No initial stresses and welded along the outer line of the bent shape.

### 1.2.4 Stress Generating

Stress was generated in the plate of the structure by a three-point bending simulation. The explicit bending analysis was followed by a springback analysis to relax the bent plate before the welding was initiated. The springback analysis removes some of the stresses from the bending operation to avoid sudden movements in the plate at the initiation of the welding. The permanent deformation of the plate was achieved by applying a load which induced high enough stresses to reach the yield strength of the stainless steel material and hence the plastic area of deformation. The material model for the finite element bending model was identical to the one employed in the modelling of the laser welding process, and will be described in section 3.5. The final stresses in the bent plate after conducting the springback analysis can be seen in figure 1.2 and 1.3. From this figure it can be seen that the highest compressive and tensile stresses in the bent steel sheet are 248.28 MPa, and

259.62, which both surpasses the yield strength of 215 MPa for the steel grade.

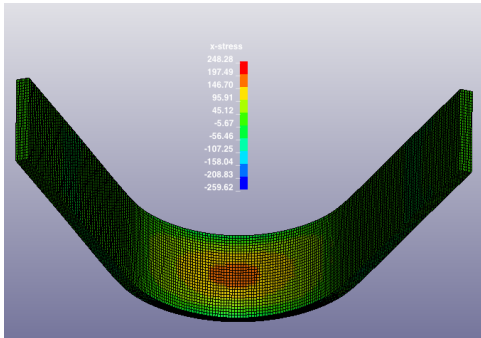


**Figure 1.2:** Compressive stresses on the bent plate for case A1 and B1.

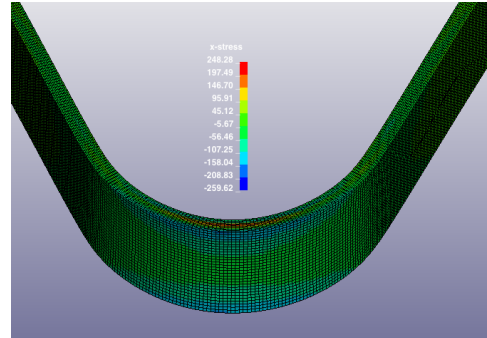


**Figure 1.3:** Tensile stresses on the bent plate for case A1 and B1.

## LITERATURE REVIEW

As the introduction states, numerical methods are widely employed for optimization and understanding of the laser welding process. The laser welding process being a complex process with coupled physical phenomena happening in the melt pool is making the numerical modelling challenging.

Several state of arts studies on the numerical approach to the laser welding process can be found in literature [4], [5], [6]. According to [4] simulating the complete phenomena occurring during the laser welding process is not yet possible, although a few at temps on the comprehensive keyhole formation can be found in literature [7], [8], [9], [10].

The numerical techniques and computer performances have matured over the last years, and the number of physical phenomena and couplings that can be taken into account in the different welding simulations have increasing significantly [11]. In literature, the so called "multi-physical" models, which aims at simulating the process impact on the temperature field with as much phenomena as possible, are extensively reported in history. [12] investigated the keyhole dynamic and shape by taking into account the heat transfer and fluid flow in solid, liquid and gas state. Investigation of the effect of keyhole formation on the liquid melt pool and weld bead were conducted by [13]. Investigation of molten pool shape and temperature field while accounting for melting and evaporation entalpy, recoil pressure, surface tension and energy loss due to evaporating materials was done by [14].

To simplify the numerical problem, the "thermo-mechanical" model is extensively employed. This model considers a simplified thermal problem and are only solving a conductive heat transfer problem and a mechanical problem, by neglecting the the multi-physic and flow effect in the molten weld pool [11].

As the figure 2.1 describes, in such models the absence of fluid flow, and hence, thermal convection are assumed to be compensated for by using a volumetric "equivalent" heat source [4]. [15] used the approach of equivalent heat source to compute the transient thermal field in thick steel plates. [15] used an equivalent heat source to simulate the heat transfer in a hybrid laser-MIG welding process.

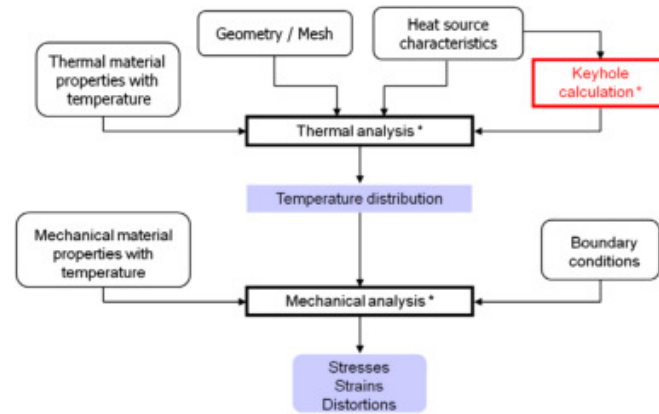


Figure 2.1: Laser welding simulation method.

[16] investigated the distortion in an aluminium plate with the use of an equivalent heat source. The difficulty with this numerical approach is to find a representation of the heat source that will give a good representation of the neglected phenomena in the weld pool.

Studies on the temperature distribution, residual stresses and distortion post welding, and the influence of different parameters and welding conditions have been reported extensively in the literature.

A numerical model to simulate the temperature field in a laser welded steel structure was done by GuoMing et al. [17]. Sun et al. compared welding induced residual stresses and distortion in thin sheet structures, from laser welding and CO<sub>2</sub> gas arc welding [18]. The results show that the laser welding process was superior in terms of both residual stresses and distortion. A comparison between experimental and finite element simulation investigation of weld pool geometry, transient temperature and distortion of laser welding of thin aluminium sheets where conducted by [19]. The result show good agreement for the comparison.

The previously presented literature studies have mainly been butt welds, but T-joint configurations have also been in the focus of several studies in literature. Buckling distortion in a thin thin walled aluminium T-joint configuration was investigated with the use of an uncoupled thermo-elastic-viscoplastic model by [20]. The effect of clamping conditions on buckling, bending, angular distortion as well as residual stresses where investigated by Schenk et al., and where found to have a great impact [21]. [22] investigated the effect of metallurgical phase change on distortion in a welded T-joint by comparison of a thermo-mechanical analysis and a thermo-metallo-mechanical analysis. The result show that including phase change has a negligible impact on distortion. [23] tried to predict the temperature field and bead geometry of a steel T-joint by investigating the effect of beam power, weld speed and beam incident angle.

Most of the developed numerical models only considered the welding process itself. As stated in the introduction, parts usually go to operations as part of the manufacturing process, which can induce stresses in the part prior to welding. This was the case for [24], where the results of the numerical methods did not match the experimental measurements well, due to the presence of residual stresses affecting the welding process. The influence of initial residual stresses on the final residual stresses after welding have been investigated by [25]. The results show that there is a significant effect. Despite this, the research conducted on initial stresses from manufacturing is limited, and to the authors knowledge there are no literature on its influence on distortion after welding.



# FINITE ELEMENT MODELING

The laser welding process was modeled using the finite element method based on conductive heat transfer and a mechanical problem. The analysis was performed as a sequential coupled thermo-mechanical model, where the heat transfer analysis was followed by the mechanical analysis. The mechanical analysis uses the nodal temperatures from the thermal analysis as input to calculate the distortion and residual stresses in the model. In figure 3.1 the sequential solver is demonstrated.

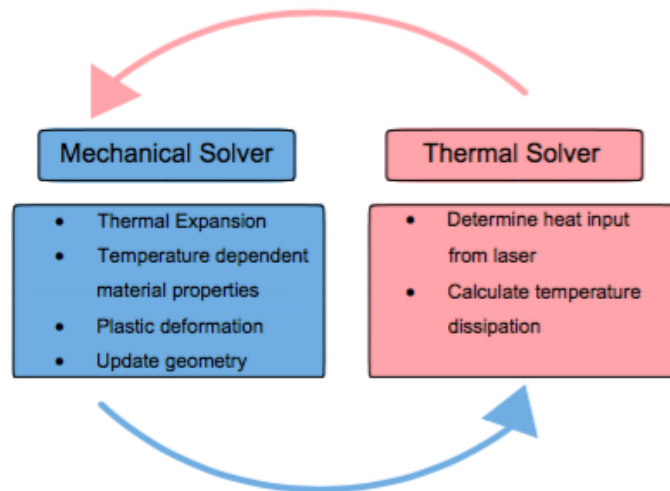


**Figure 3.1:** illustration of the coupled thermo-mechanical analysis strategy.

Calculations and analysis was performed using LS-DYNA finite element code, while LS-PrePost (4.7) was employed for the pre and post-processing. The complete keydeck, except for node and element data is presented in Appendix A. For the entire numerical calculations, the unit system (b) was used according to LS-DYNA Manual [26].

### 3.1 Assumptions and exclusions

As stated in the introduction, laser welding is a complex process and the whole phenomena is not yet possible to simulate [4]. To keep the model simple, some assumption and exclusion made for the model will be presented:

- The initial temperature of the model is set to the ambient surrounding temperature.
- Radiation and convection heat loss from the surface of the workpiece are taken into account.
- The fluid flow and convection in the molten weld pool are neglected. To compensate for the effect of fluid flow, an equivalent volumetric heat source generates the heat inside the material.
- Thermo-physical properties of the material are given as a function of temperature.
- Surface forces and plasma pressure are excluded.
- Laser-material interaction and absorption mechanisms are neglected.
- Laser-arc distance and synergy effects are excluded.

### 3.2 Thermal conduction model

For the calculation of the temperature distribution Fourier's equation for three dimensional heat conduction was used. This equation with temperature dependent material properties is given by the following partial differential equation:

$$\rho c(T) \frac{\delta T}{\delta t} = \frac{\delta}{\delta x} \left( k(T) \frac{\delta T}{\delta x} \right) + \frac{\delta}{\delta y} \left( k(T) \frac{\delta T}{\delta y} \right) + \frac{\delta}{\delta z} \left( k(T) \frac{\delta T}{\delta z} \right) + q_v \quad (3.1)$$

In the above equation  $q_v$  is the volumetric internal energy generation;  $T$  is the temperature;  $x, y$  and  $z$  represent space coordinates;  $t$  represents time;  $\rho$  is the density of the material;  $c$  the specific heat and  $k$  is the thermal conductivity coefficient.

### 3.3 Heat source model

The proper selection of heat source is critical to get an accurate thermal distribution and hence geometric distortion and stresses. Different studies have for this reason been conducted with a focused on finding a simple and reliable heat source [27], [28], [29].

Various volumetric heat source models have been proposed for the laser welding process, two of these heat sources that are widely known and commonly used are the double ellipsoidal volumetric heat source [30] and the three dimensional conical heat source [31]. The double ellipsoidal heat source model was originally intended to be suited for both shallow welds made by arc welding processes and deeper penetration welds resulting from high power density processes.

This relatively simple heat source model considers a Gaussian heat intensity distribution along the thickness of the workpiece. It combines two ellipsoids for the heat distribution, as it was discovered through experiments that the temperature gradient in front of the moving heat source differed from the one trailing behind it. This introduced the two fractions  $f_f$  and  $f_r$  of the heat deposit in the front and rear quadrants, where  $f_f + f_r = 2$  [30]. The power density distribution inside the front and rear quadrant of the moving arc heat source, as seen in figure 3.2, can mathematically be expressed by the equation:

$$q_f(x, y, z, t) = \frac{6\sqrt{3}f_f Q}{abc\pi\sqrt{\pi}} e^{-3x^2/a^2} e^{-3y^2/b^2} e^{-3[z+v(\tau-t)]^2/c^2} \quad (3.2)$$

$$q_r(x, y, z, t) = \frac{6\sqrt{3}f_r Q}{abc\pi\sqrt{\pi}} e^{-3x^2/a^2} e^{-3y^2/b^2} e^{-3[z+v(\tau-t)]^2/c^2} \quad (3.3)$$

where, the parameter  $a$  represents half the ellipsoid width,  $b$  represents the depth and  $c$  the length of the ellipsoid. The parameters can be seen in figure 3.2, which represents the heat flux distribution by a double ellipsoid heat source model.

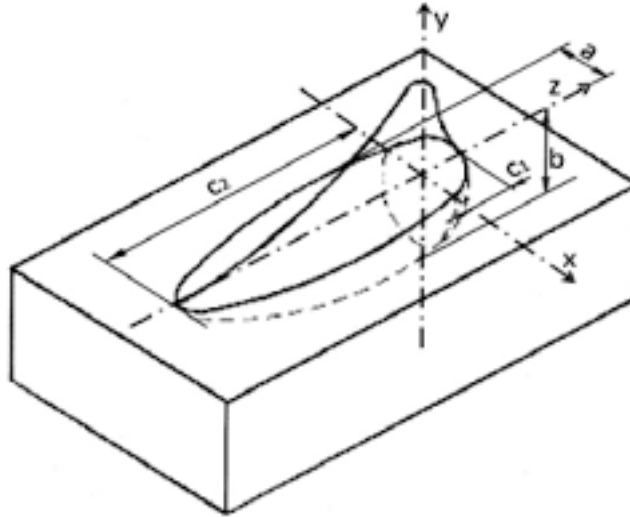


Figure 3.2: Double ellipsoid heat source model [32]

The conical heat source model, seen in figure 3.3 was proposed as the power distribution of the double ellipsoidal heat source model was not applicable to welding process with very high width to depth ratio. This model has a constant power density in the shape of a cone, with the maximum power density region at the

top that linearly decreases to a minimum at the bottom [31]. The mathematical expression for the power density distribution are given as:

$$Q_v(r, z) = Q_0 \exp\left(\frac{-3r^2}{r_0^2}\right) \quad (3.4)$$

where,  $Q_v$  represents the total volumetric heat flux,  $Q_0$  represent the maximum value of the heat flux,  $r$  is the radius of the cone as a function of Cartesian coordinates  $x$  and  $y$ . The distribution parameter for the cone as a function of depth ( $z$ ),  $r_0$ , can be expressed as

$$r_0(z) = r_e - (r_e - r_i) \frac{z_e - z}{z_e - z_i} \quad (3.5)$$

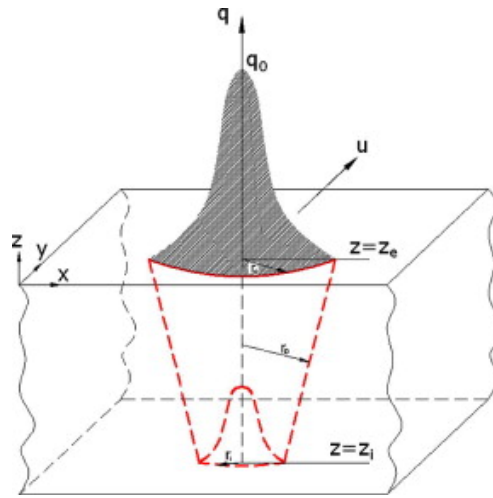


Figure 3.3: Three dimensional conical heat source [32]

### 3.3.1 Laser welding and heat source parameters

For the numerical modeling of a heat source the weld pool geometry must be pre-defined as its dimensions physically are the same as the heat source's. Predicting the weld pool geometry is no easy task, with several interacting parameters influencing the dimensions. The three main variables that must be considered are:

- Laser power
- Travel speed
- Focal point position

The process parameters and their effect have been well documented in the literature. Both predicting the pool geometry and optimization of the welding conditions by developing mathematical models and numerical methods have been reported [33], [34], [35], [36] [37], [38], [33], [39]. Finding a model that works across different design geometry and material models have proven to be difficult, but the effect and correlation of the welding parameters and the weld pool geometry have been identified.

The weld speed have great influence of the size of the weld pool, high velocity gives a smaller melt pool. The weld pool becomes narrow and shallow due to the low interaction time between the metal and laser beam. Increasing the laser power have the opposite effect as it produces higher heat input, which results in deeper penetration [38].

Most research use experimental data to define the weld pool geometry and calibrate the numerical models accordingly. During this study no experimental laser welding for comparison of the weld pool were conducted and the weld parameters defining the weld pool geometry are set according to prior researchers' work. For validation of the model a set of fitting welding parameters are selected based on geometry and material.

The finite element model will be validated against two sets of welding parameters. As discussed the parameters influence the final result on the weld and could have an impact on the distortion as well.

The first set of welding parameters replicates a study who used numerical simulation to design welding parameters for laser welding of thin stainless steel AISI 304 tubes, with a thickness of 0.8 mm. With the use of a volumetric heat source this study investigated the influence of welding parameters and verified the numerical results experimentally [40]. For this purpose a conical heat source was chosen to describe the heat distribution of the laser beam, with the parameters seen in table 3.1.

$r_i$	$r_e$	$z$
0.3	0.2	1.0

**Table 3.1:** Conical heat source parameters.

A previous student project simulated a laser welding process on a T-joint with a plate thickness of 1.5mm and material EN-1.4301, with the use of a double ellipsoidal heat source [3]. The welding conditions from this study can be reproduced exactly, except for the angle of the laser beam, where the weld went through the stiffener plate.

As presented in section 3.3 the double ellipsoid heat source consists of four parameters that must be determined. Goldak et al. suggested that it is reasonable to take half the length of the frontal ellipsoid as half the weld width and the length of the rear as twice the weld width. The best correspondence between measured and the calculated results for the fractions  $f_f$  and  $f_r$  was found to be when set to 0.6 and 1.4, respectively [30]. This was implemented by [3] and the predicted heat source parameters are seen in table 3.2, below.

$a$	$b$	$c_f$	$c_r$	$f_f$	$f_r$
0.64	3.4	0.64	2.56	1.4	0.6

**Table 3.2:** Goldak double ellipsoid heat source parameters.

The described studies had an incidence angle of  $90^0$  for the laser beam, which is not applicable in the current numerical model. In a study by [23], the beam angle was investigated and optimized for laser welding on a stainless steel AISI 304 T-joint, of 1.6 mm thickness. An incidence angle of 60 degrees gave the best results and will be used in the finite element model, seen in figure 3.4. It should be noted that [23] welded the structure from both sides, which might effect the optimized incidence angle of the laser beam.

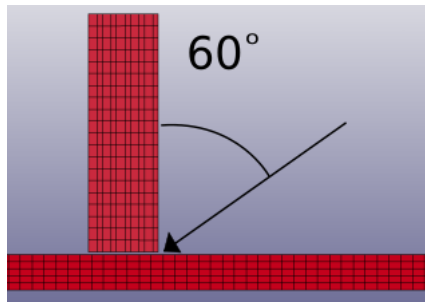


**Figure 3.4:** Incidence angle of the laser beam.

The welding parameters used together with the Goldak and conical volumetric heat sources are presented in table 3.3.

	Power [kW]	Speed [mm/min]	Angle
<b>Conical</b>	1.25	500	60
<b>Goldak</b>	1.42	1200	90

**Table 3.3:** The laser welding parameters with the volumetric heat sources.

### 3.4 Thermal boundary conditions

In order to find the general solution for differential equation 3.1, boundary and initial conditions must be specified. The initial condition at  $t = 0$  the work piece have a uniform primary temperature, which are set to the ambient temperature  $T_0$  of 293K as following:

$$T(x, y, z, 0) = T_0(x, y, z) \quad (3.6)$$

During the laser welding process the work piece exchange heat with the ambient surroundings, due to the significant difference in temperature. This heat loss from all free surfaces boundaries of the work piece, to the ambient air, happens in the form of radiation and convection [41].

Heat loss by the means of convection is heat transfer through movement of molecules, diffusion and fluid motion, caused by temperature difference. The phenomena can be either natural or forced, the latter being external forces influencing the flow rate, increasing the convection rate. In this model, forced convection is assumed due to having an flow of air to keep residue from entering the laser during the welding process.

This form of heat transfer is only dependent on the convective heat transfer coefficient of the material and the temperature difference, given by Newton's law:

$$q_c = -h(T - T_0) \quad (3.7)$$

Where  $q_c$  is the heat loss from the work piece surfaces due to conduction, given in  $W/m^2$ ,  $h$  is the constant convective coefficient.  $T_0$  is as stated the ambient temperature and  $T$  the temperature of the work piece.

Heat loss by means of radiation is energy emitted by the object through electromagnetic waves to the ambient air [42], and given by the equation:

$$q_{rad} = -\epsilon\sigma(T^4 - T_0^4) \quad (3.8)$$

Also given in  $W/m^2$ , with  $\sigma$  being Stefan Boltzmann constant and  $\epsilon$  is the emissivity factor for the material, that provides a measure of the energy emitted from the surface relative to a black body [43].

The values used for the heat transfer coefficient and radiation constants are given as:

- convective heat transfer coefficient for air flow,  $h_{forced} = 0.1 \frac{mW}{Kmm^2}$  [44]
- Emissivity of steel surface,  $\epsilon = 0.8$  [45].
- Stefan Boltzmann constant,  $\sigma = 5.67 \times 10^{-8} W/m^2K^4$ .
- Thermal contact conductance coefficient,  $h_{cond} = 16.2$  [46]

Additionally, thermal contact between the plates are used to account for the complex nature of the thermal boundary conditions in the model. The contact is defined by the keyword CONTROL\_CONTACT-AUTOMATIC\_SURFACE\_TO\_SURFACE\_TIED\_WELD, which is a two way contact, where the slave nodes are constrained to move with the master surface [26]. When including the thermal option of the keyword, the keyword will tie the selected surfaces together if the temperature of the surfaces rises above the lateral heat of the material. This keyword also accounts for the presence of thermal conductance between the interface of the parts during the welding process.

There is a slight gap between the two parts to be welded together, as they could not be aligned perfectly. This is accounted for in the contact definition as well, as it allows for setting a maximum distance where nodes on each of the parts to be welded together, within this distance, will be tied together. The gap can be seen in figure ?? as cross-sections of the model at different lengths along the x-direction of the Stiffener.

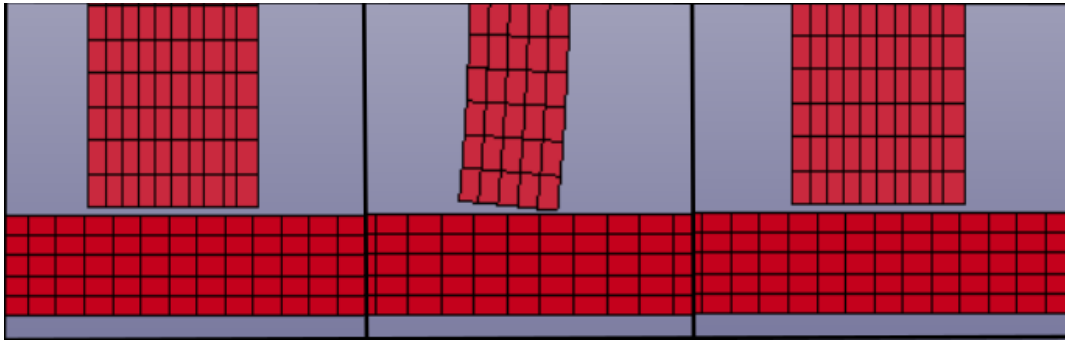


Figure 3.5: Caption

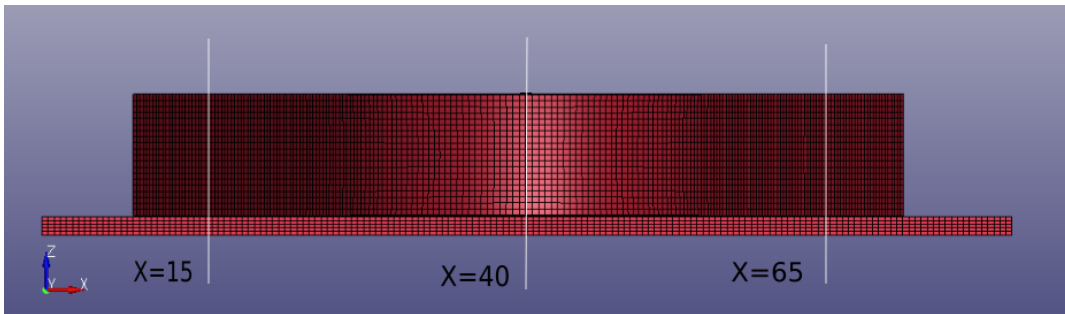


Figure 3.6: Illustration of where along the x-axis of the model the gaps in figure ?? can be found.

The figure 3.6 illustrates the cross-sections, at  $x=15$ ,  $x=40$  and  $x=65$ , respectively. As can be seen in figure 3.5 the gap is largest along the back of the bent shape and reaches it maximum at  $x=40$ . The maximum distance to close this gap between the two surfaces during welding is set to 0.5 mm to ensure the surfaces being tied together along the complete weld path.

### 3.5 Material model

To accurately model the thermal-mechanical behaviour during welding, temperature dependent material properties are used in the numerical model. For the thermal solver, thermal conductivity and heat capacity have been considered to be temperature dependent, as shown in figure 3.7

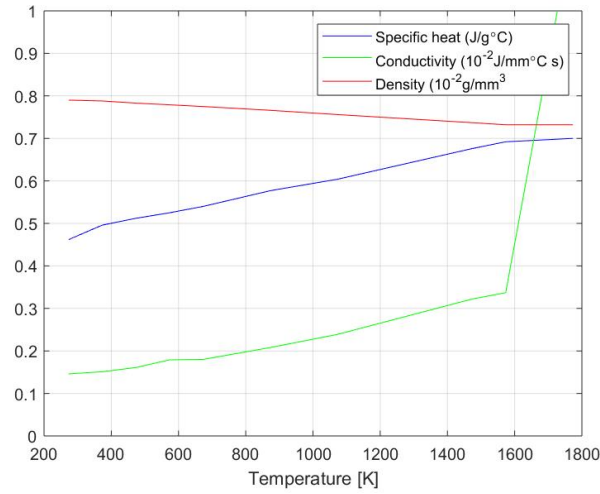


Figure 3.7: Temperature dependent thermal physical material properties of STEEL

The mechanical properties was modeled using a thermo-elastic-plastic model with kinematic hardening. This model uses temperature dependent material properties for Young's moduli, Poissons' ratio, thermal expansion coefficient, yield stress and plastic hardening modulus, seen in figure 3.8, to calculate the mechanical response to temperature change.

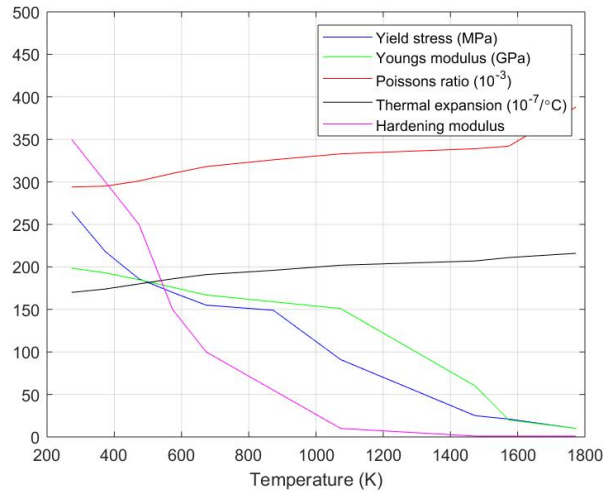


Figure 3.8: Temperature dependent mechanical properties of STEEL

The required material properties, except for the hardening modulus, were obtained from [47]. The hardening modulus is obtained by solving the Holloman's equation for true strain and stress given as:

$$\sigma = K + \varepsilon^n \quad (3.9)$$

where,  $\sigma$  represents the stress applied to the material,  $\varepsilon$  represents the strain,  $K$  is the strain-hardening coefficient and  $n$  the the strain-hardening exponent. []

approximated the strain hardening modulus for the strain value 0.1 and result are used in this model.

The material models are set up with the keywords `*MAT_CMW` and `*MAT_THERMAL_CWM` in LS-DYNA. These are specific welding material models, which allows for material creation and annealing. The state of the material is given by an activation temperature where a solid state is given a very low activation temperature and the liquid phase activation temperature is typically the melting temperature of the material. The annealing functionality is implemented to simulate a limiting temperature where history variables as effective plastic strain and back stress are zeroed out [48].

## 3.6 Numerical model

The full size specimen was considered for the finite element models for the laser welding process. Although, using symmetry to save computational cost be beneficial to do so would not give the full extent of the displacement in the structure post welding.

### 3.6.1 Elements

The element formulation is set to be 8-node fully integrated S/R elements under keyword `*SECTION-SOLID` in LS-DYNA pre-post. Solid elements are three dimensional finite elements that can model bodies and structures without any a prior geometric specification. This benefit of this element behavior is not needing any hourglass control, as there are no zero-energy modes. Fully integrated elements are computationally costly but give accurate results [49].

### 3.6.2 Discretization

The discretization of the finite element model is an of great importance in the model setup as it significantly effects the accuracy of the results. The minimum discretization requirements must be met for the model to compute an accurate description of heat flow for the welding process. If excessive degrees of freedoms are present in the model the computational time will be lengthy, hence a balance that insure a sufficient solution and at the same time comes with an acceptable simulation time must be determined. The element size is especially crucial along the weld, where the temperature gradients are steeper, and the element size should be chosen accordingly.

[50] investigated the sufficient number of elements in a finite element model based on three requirements.

1. Spatial discretization: the number of elements per radius of the laser spot. This number will determine the total number of DOF.
2. Temporal discretization: the number of time increments per radius.

### 3. Meshing density through thickness: number of elements in the thickness direction

This research found that increasing the number of elements after 2 per radius and three through the thickness would not significantly increase the accuracy. The number of time increments was found to have a good accuracy at four per time step.

Following the guidelines of [50] the time to complete the analysis proved to become impractically large. To obtain an appropriate mesh density for the finite element model, the intention was to have the simulation of the laser welding process performed considering two different mesh models for comparison. Due to time issues only one of the mesh model was considered.

Two identical models with different element size were supposed to be set up to investigate the mesh density necessary to achieve sufficient accuracy. Both models with element size, number of elements and nodes are presented in table 3.4, where the model 1 with coarser mesh was used for the finite element model. The meshed structure are shown in figure 3.9 and a detailed view of the element size in the mesh, in figure 3.10.

Model	Nr of elements	Number of node	Element dimensions bent plate	Element dimensions stiffener
1	43 650	58 540	0.67x0.67x0.3	0.67x0.67x0.5
2	116 000	142 212	0.5x0.5x0.3	0.5x0.5x0.3

**Table 3.4:** Mesh models with their elements and dimensions.

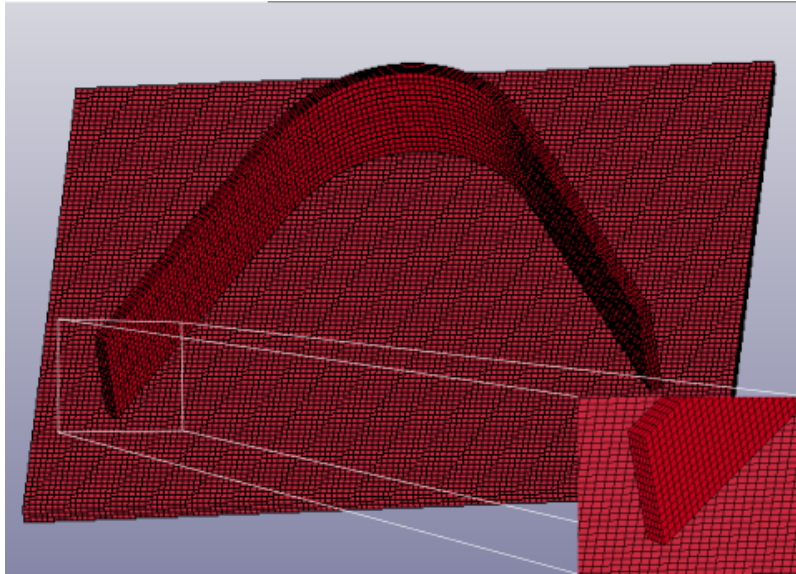


**Figure 3.9:** Finite element model of the structure with detail view of the mesh 1.

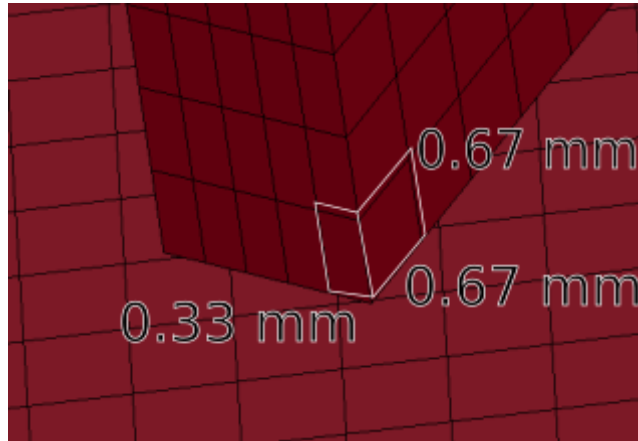


Figure 3.10: Detailed view of the element size of mesh 1.

### 3.6.3 Implicit

Implicit time integration is used as a solver for this study. The solution is obtained in a number of steps, and the solution for the current time step is based on the solution from the previous. A large numerically effort is required to form, store and invert the system of equations, but implicit solutions have the advantage of being unconditionally stable and facilitate larger time steps [51].

### 3.6.4 Time step

The proper selection of the time step is of great importance for the accuracy and stability of the thermal solver. The time step should be calculated in accordance with the element size, where this relationship is especially important in the regions of the weld where the thermal gradients are high [52].

The critical value of the time step in regions with severe thermal gradients are given as a relationship between the element size ( $\Delta x$ ) and thermal diffusivity:

$$\Delta t = 0.25 \frac{\Delta x^2}{\alpha} \quad (3.10)$$

where

$$\alpha = \frac{k}{\rho C_p} \quad (3.11)$$

The thermal diffusivity,  $\alpha$  of the material is the ability to transport heat through conduction ( $k$ ) relative to the ability of storing it ( $\rho * C_p$ ) and are dependent on the thermal physical properties of the material [52]. The time step is determined by using the thermal diffusivity at the melting temperature ( $0.234 \text{ mm}^2/\text{s}$ ). Substituting this value in Eq. 3.10 the time step calculated for the element size of 0.5 is  $\Delta t = 0.28 \text{ s}$ . This time step was used for the entire numerical calculation, where the time step for the model is variable, allowing smaller time step to be used in the analysis, but forces the solver to stay below the set value.

### 3.6.5 Weld

The heat source model is implemented in the numerical analysis by implementing the keyword `*BOUNDARY_THERMAL_WELD_TRAJECTORY` in the model. This keyword includes several different heat sources models to choose from and options for defining the weld. The trajectory of the weld are set by nodes, where the laser beam will trace the nodes in the set order, hence letting the user define the weld from starting point to end point. The possibility of choosing the angle of the laser beam are done by having a segment set, which the laser beam are perpendicular to, unless otherwise stated. The angle are changed by using a curve where the angle are time dependent. The nodes for the trajectory and the segments for the direction can be seen in figure 3.11 for the Case A and figure 3.12 for Case B.

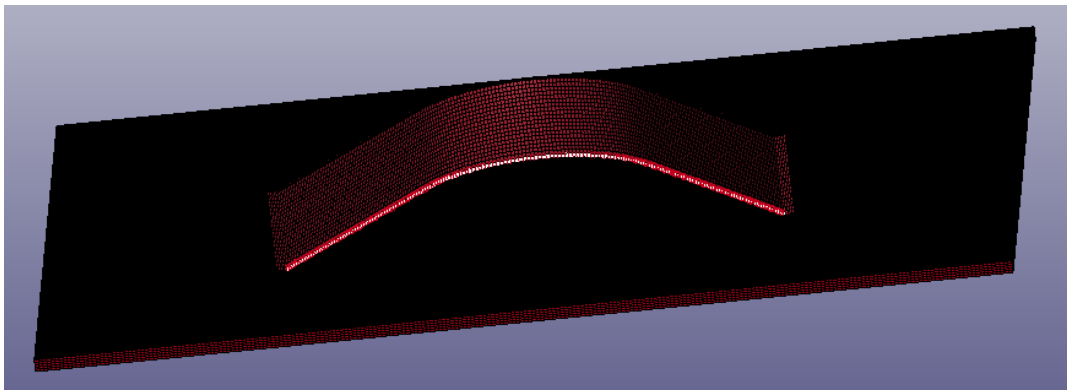


Figure 3.11: Nodes and segments indicating the weld placement.

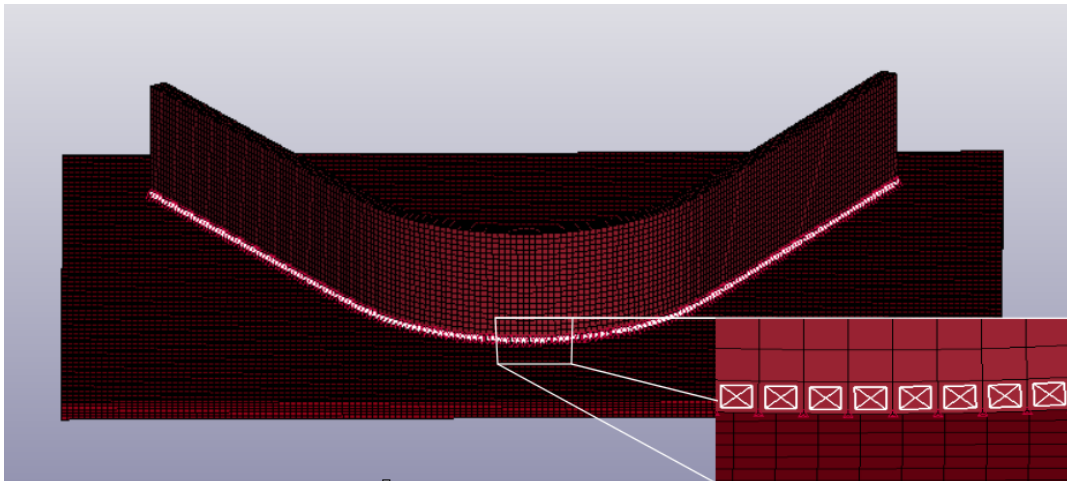


Figure 3.12: Nodes deciding the laser beam path and segments the laser beam will be normal to.

To control the heat input, a curve that defines the heat input according to time is used. The welding is completed in the first 5 seconds and 3.333 seconds for the welding parameters set 1 and 2, respectively, of the total 20 seconds long simulation.

### 3.6.6 Model boundary conditions

The workpiece is fixed in space, with three of the workpiece's sides mechanically constrained against movement.

The only constraint on the stiffener plate should be sufficient support the plate in the right position during welding and restricts movement in all directions, but are free to rotate around all axes. This one is applied along the x-axis on the edge on the backside of the bent shape, shown in figure 3.13

The bent plate are more constrained as it is more prone to movement during welding initiation. The upper edge is constrained for all translation and rotation, except translation in the z-direction. The vertical edge where the weld is initiated, is restrained in all six degrees of freedom. These constraints are illustrated in figure 3.14

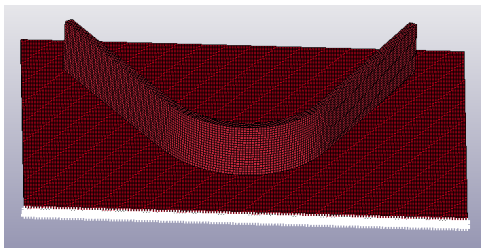


Figure 3.13: Constraints on the stiffener.

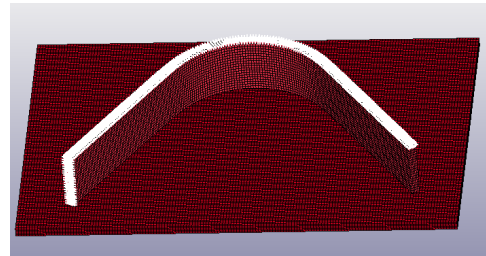


Figure 3.14: Constraints on the bent plate.

# RESULTS AND DISCUSSION

## 4.1 Goldak double ellipsoidal heat source

### 4.1.1 Case A1 and A2

The computed temperature distribution of the three dimensional finite element model can be seen in figure 4.1- 4.6 with a laser power of 1,42 kW, a welding speed of 20 mm/s, an incident angle of  $60^0$  and the laser beam tracing along the inside of the bent plate. The temperature legend is dynamic, to properly display the temperature distribution during the cooling time after the laser welding process in completed after 5.0 seconds.

The temperature in the weld pool where the laser beam is positioned is around 3300 K, fluctuating slightly between time steps. The temperature is not constant throughout the laser welding process, which is probably due to the element size or time step is too large to accurately describe the temperature field in the finite element model.

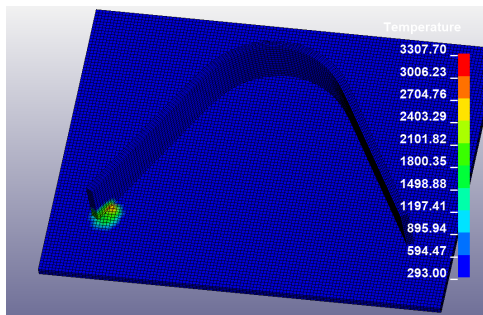


**Figure 4.1:** Temperature distribution 0.2 seconds after welding initiation.

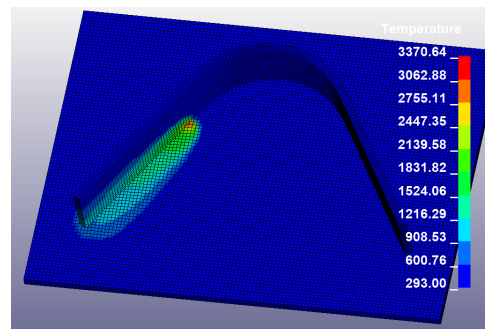


**Figure 4.2:** Temperature distribution 1.5 seconds after welding initiation.

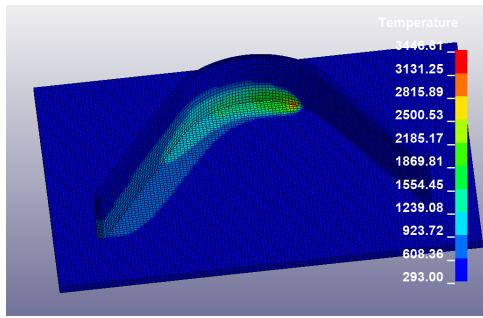


**Figure 4.3:** Temperature distribution 3.0 seconds after welding initiation.

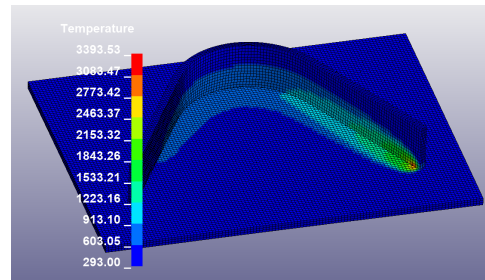


**Figure 4.4:** Temperature distribution 5.0 seconds after welding initiation.

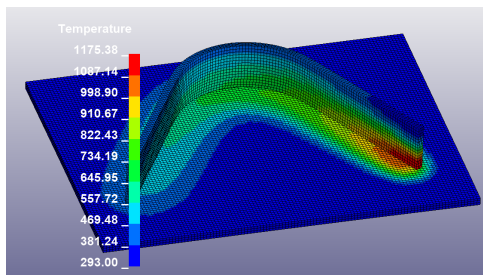


**Figure 4.5:** Temperature distribution 1 second after weld completion.

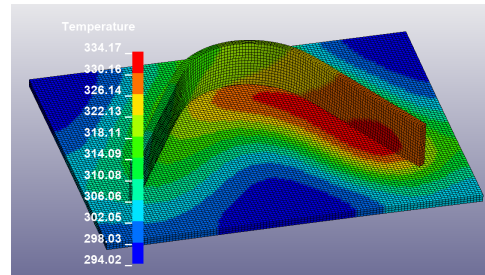


**Figure 4.6:** Temperature distribution 15 seconds after weld completion.

### Distortion

Figure 4.7 - 4.14 shows a sample of vector plots of displacement occurring in the finite element model during the laser welding process, allocated in the X-direction. The column to the left presents the displacement in Case A1 and the column to the right Case A2, for comparison. The displacement legend is static to present a comparison of the displacement vectors during different times of the laser welding process.

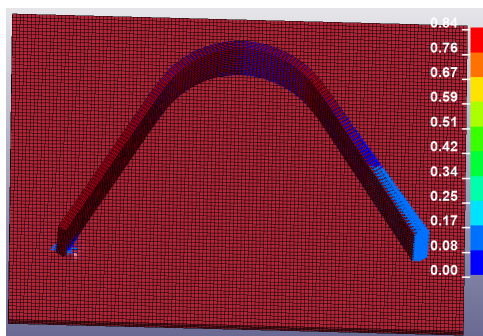


**Figure 4.7:** Vector displacement for Case A1 0.2 seconds into the laser welding process.

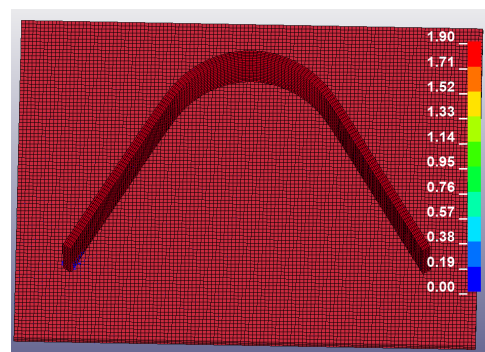


**Figure 4.8:** Vector displacement for Case A2 0.2 seconds into the laser welding process.

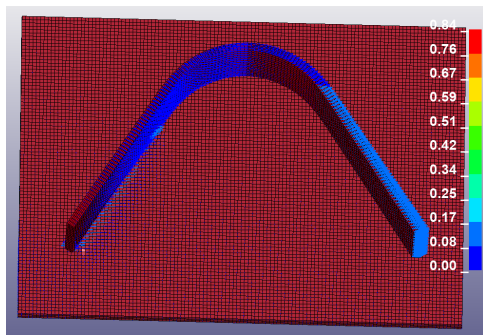


**Figure 4.9:** Vector displacement for Case A1 1.5 seconds into the laser welding process.

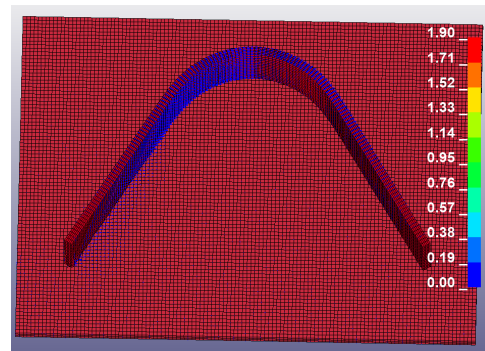


**Figure 4.10:** Vector displacement for Case A2 1.5 seconds into the laser welding process.

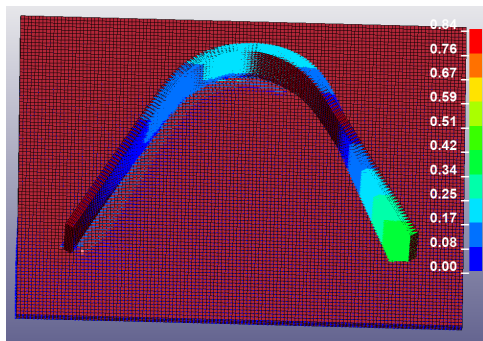


**Figure 4.11:** Vector displacement for Case A1 3.0 seconds into the laser welding process.

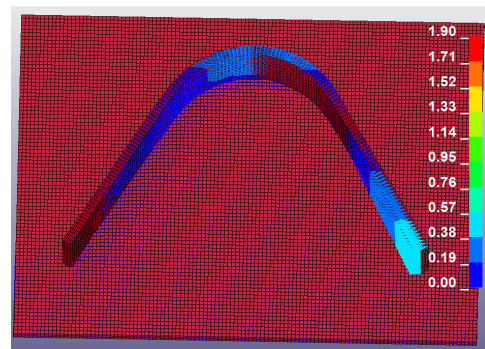


**Figure 4.12:** Vector displacement for Case A2 3.0 seconds into the laser welding process.

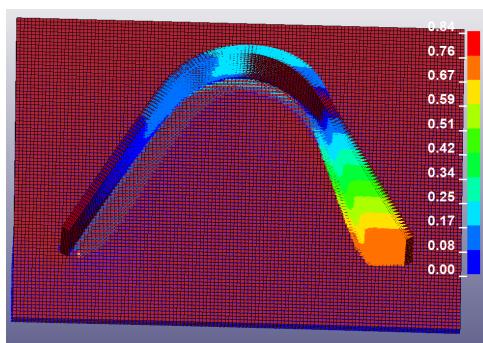


**Figure 4.13:** Vector displacement for Case A1 as the welding is completed.

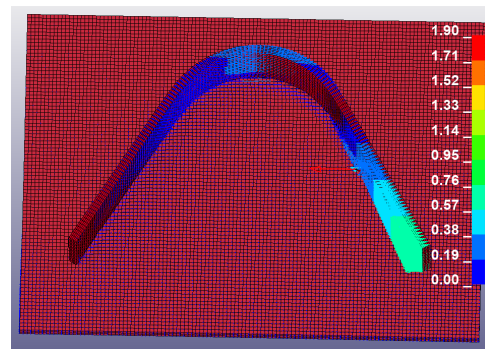


**Figure 4.14:** Vector displacement for Case A2 as the welding is completed.

Comparing the vector plots of displacement in Case A1 to case A2, it can be seen that the displacement are very similar in both cases. The opposite end of the weld initiation of the bent plate is slightly displaced outwards the first 1-2 seconds of the welding process. As the laser beam approaches the bent area of the plate it can be seen that the plate is retracting and keeps on doing so even during the cooling stage, when the welding is completed. The simulation of the

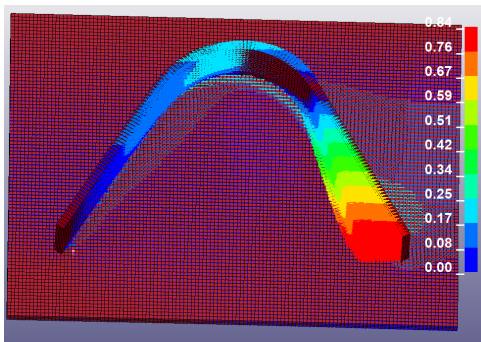


Figure 4.15: Vector displacement for Case A1 20 seconds after welding initiation

structure without initial stresses was stopped after the welding was completed and the measurements will be done at this time.

The final distortion of the bent plate are found by measuring the distance between nodes at each end of the bent plate of the finite element model, prior and post the laser welding process. The initial distance between the edges of the bent plate was 61.0561 mm. Figure 4.16 and 4.17 presents the distance between the top nodes at each edge as well as the bottom ones after welding is completed. In Case A1, where there are initial stresses present in the finite element model, the laser welding process creates distortion in the bent plate of the magnitude 0.641 mm. In Case A2, with a stress free structure prior to welding the distortion reaches 0.745 mm.

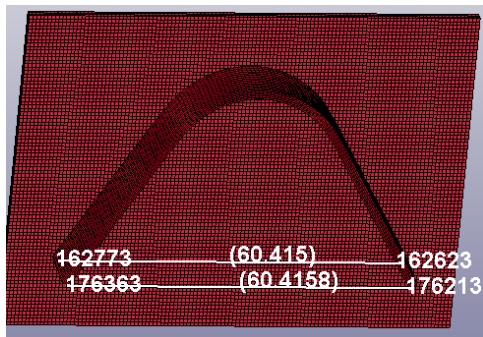


Figure 4.16: Distance between nodes at the edges of the bent plate after welding in Case A1.

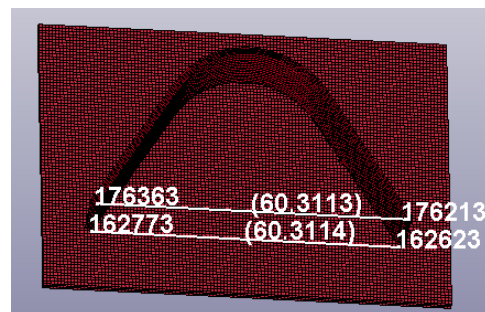
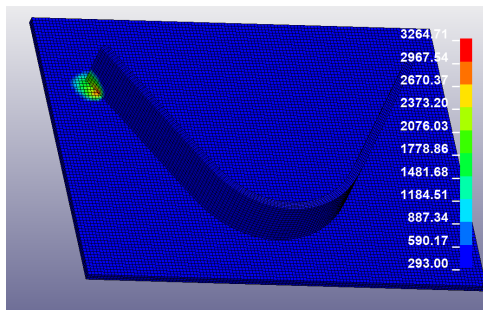


Figure 4.17: Distance between nodes at the edges of the bent plate after welding in Case A2.

### Case B1 and B2

The computed temperature distribution of the three dimensional finite element model can be seen in figure 4.18-4.23 with a laser power of 1,42 kW, a welding speed of 20 mm/s, an incident angle of  $60^{\circ}$  and the laser beam tracing along the outside of the bent plate. The temperature field and cooling rate are similar to those in Case A1 and A2, the temperature in melt pool are about 3300 K and are fluctuating slightly.



**Figure 4.18:** Temperature distribution 0.2 seconds after welding initiation.

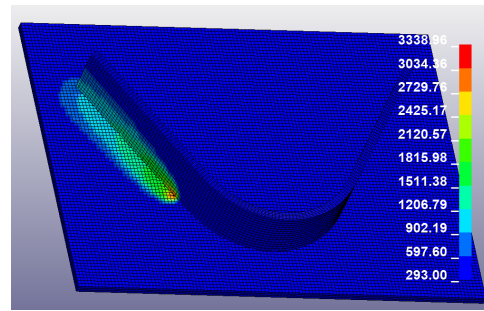


**Figure 4.19:** Temperature distribution 1.5 seconds after welding initiation.

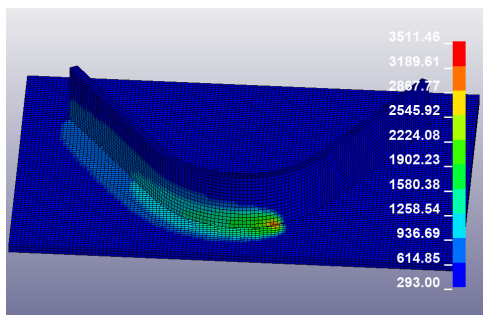


**Figure 4.20:** Temperature distribution 3.0 seconds after welding initiation.

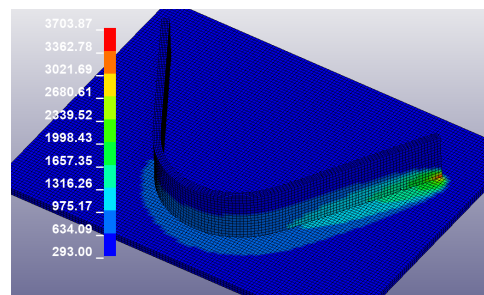


**Figure 4.21:** Temperature distribution 5.0 seconds after welding initiation.

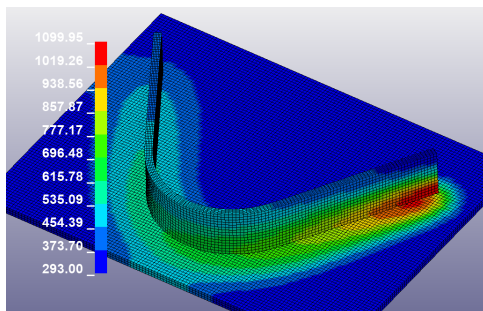


**Figure 4.22:** Temperature distribution 15 second after weld completion.

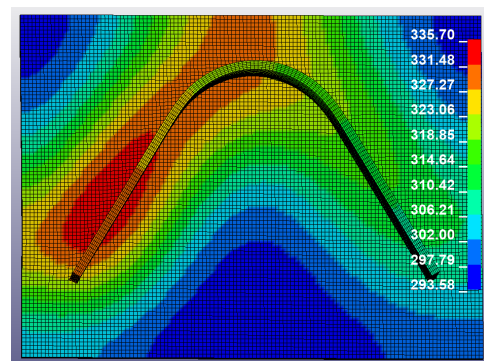


**Figure 4.23:** Temperature distribution 15 seconds after weld completion.

### Distortion

The distortion allocated in the X-direction for Case B1 and Case B2 during the laser welding are presented in figure 4.24 - figure 4.31.

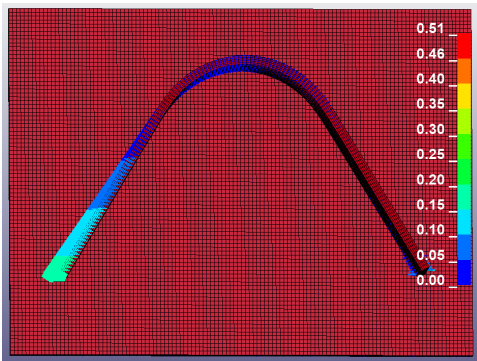


**Figure 4.24:** Vector displacement for Case B1 0.2 seconds into the laser welding process.

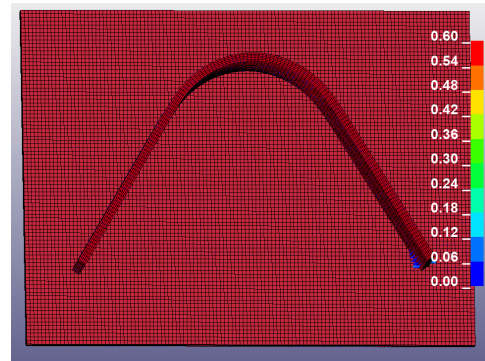


**Figure 4.25:** Vector displacement for Case B2 0.2 seconds into the laser welding process.

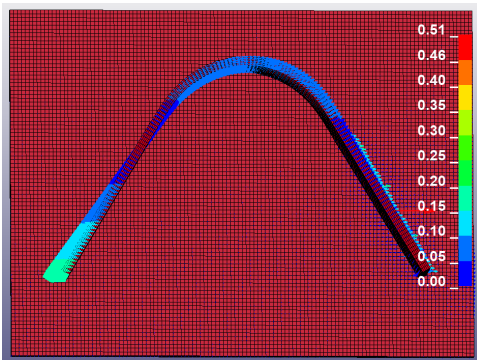


**Figure 4.26:** Vector displacement for Case B1 1.5 seconds into the laser welding process.

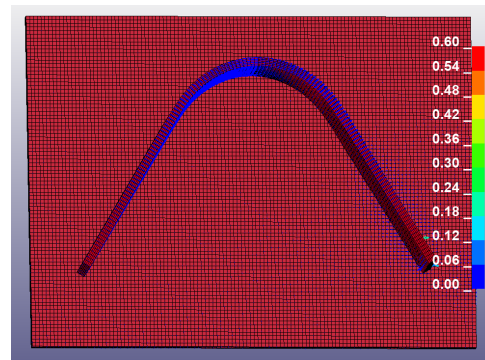


**Figure 4.27:** Vector displacement for Case B2 1.5 seconds into the laser welding process.

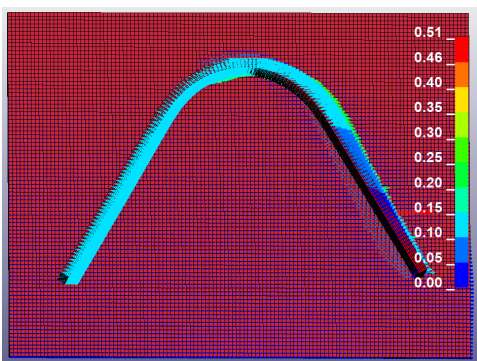


**Figure 4.28:** Vector displacement for Case B1 3.0 seconds into the laser welding process.

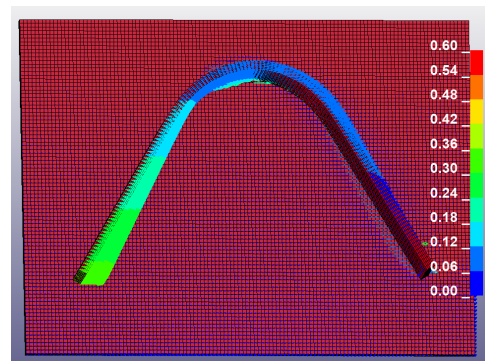


**Figure 4.29:** Vector displacement for Case B2 3.0 seconds into the laser welding process.

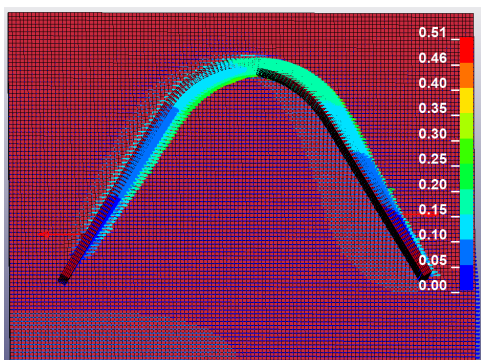


**Figure 4.30:** Vector displacement for Case B1 as the welding is completed.

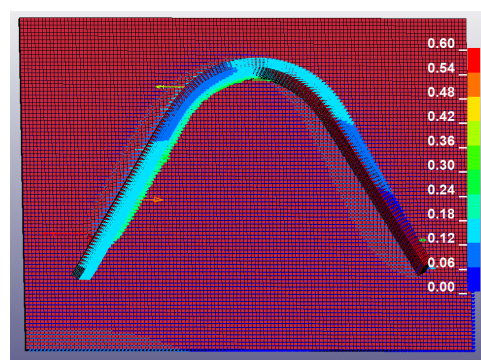


**Figure 4.31:** Vector displacement for Case B2 as the welding is completed.

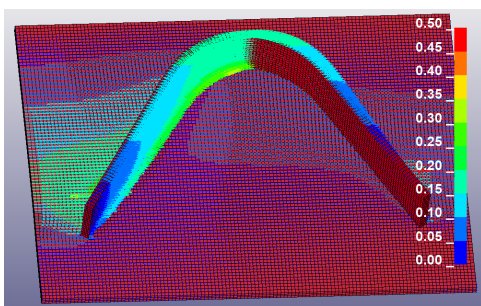


**Figure 4.32:** Vector plot of displacement for Case B1 20 seconds after welding initiation.

The displacement pattern are similar to the the models welded from the inside of the bent plate. At the first seconds of the laser welding process the displacements are slightly larger in the structure with initial stresses. However, towards the end of the welding process the displacement seems to get larger at the end of the bent plate in Case B2, while in B1 the displacement is less.

The distance between the edges of the bent plate for Case B1 and B2, post welding, are shown in figure 4.33 and 4.34, respectively. Having an initial distance as the same as in Case A1 and A2, the distortion in Case B1 are calculated to 0.0005 mm. The bent plate in Case B2 are mores distorted with a magnitude of 0.172 mm.

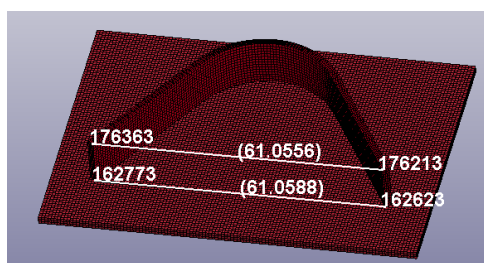


**Figure 4.33:** Distance between nodes at the edges of the bent plate after welding in Case B1.

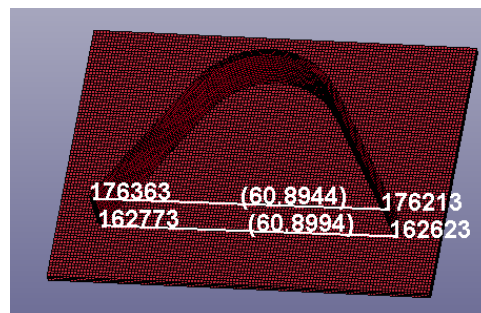


**Figure 4.34:** Distance between nodes at the edges of the bent plate after welding in Case B2.

## 4.2 Conical heat source

### 4.2.1 Case A1 and A2

The computed temperature distribution of the three dimensional finite element model can be seen in figure 4.35-4.40 with a laser power of 0.80 kW, a welding speed of 30 mm/s, an incident angle of  $60^{\circ}$  and the laser beam tracing along the inside of the bent plate.

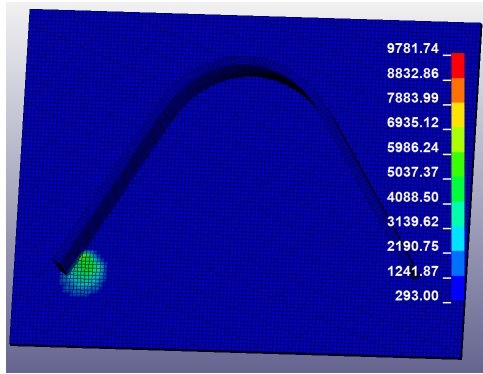


**Figure 4.35:** Temperature distribution 0.2 seconds after welding initiation.

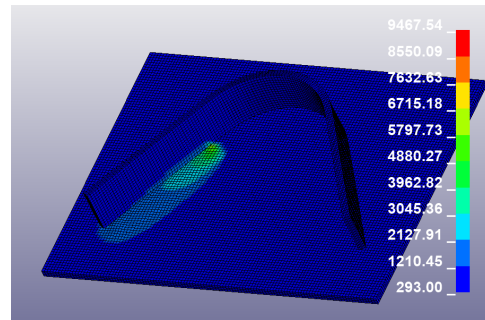


**Figure 4.36:** Temperature distribution 1.0 seconds after welding initiation.

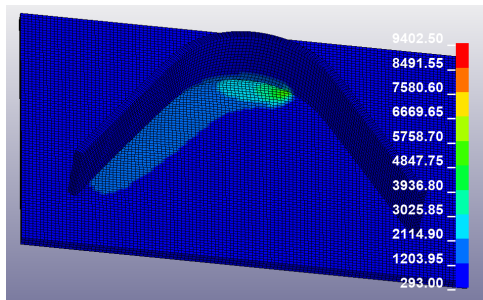


**Figure 4.37:** Temperature distribution 2.0 seconds after welding initiation.

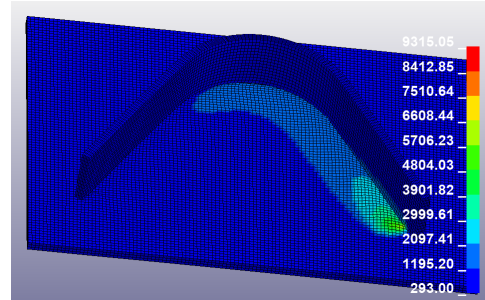


**Figure 4.38:** Temperature distribution 3.3 seconds after welding initiation.

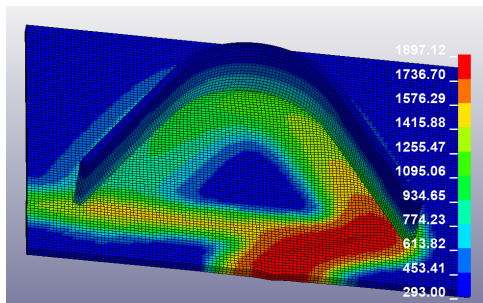


**Figure 4.39:** Temperature distribution 3.0 seconds after welding initiation.

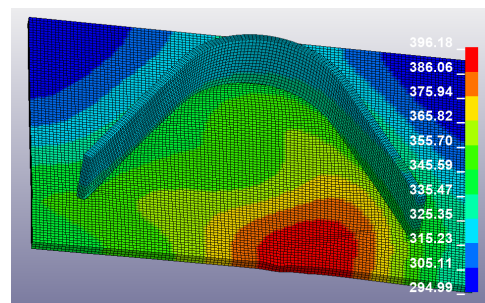


**Figure 4.40:** Temperature distribution 5.0 seconds after welding initiation.

The temperature in this model is high, it reaches above 9000 degrees. The welding speed is higher and the laser beam power is lower than for the other set of laser welding parameters, which should indicate lower temperature gradients. As this is not the case it could be a result of the heat source chosen. The heat input is also unexpected as it seems to be higher on the bottom of the stiffener, as seen in figure 4.41.

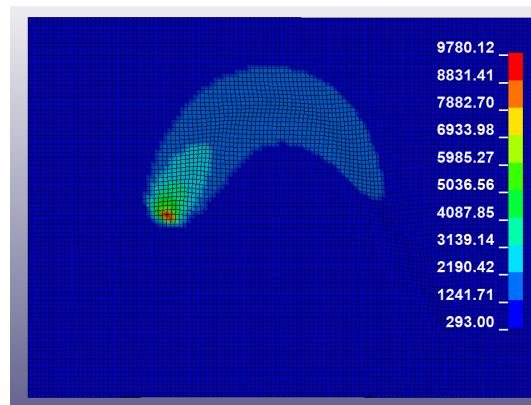


Figure 4.41: Caption

## Distortion

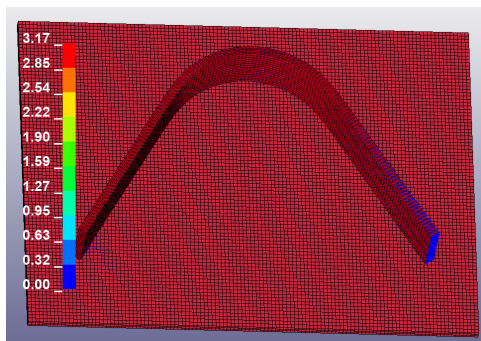


Figure 4.42: Vector displacement for Case A1 0.2 seconds into the laser welding process.

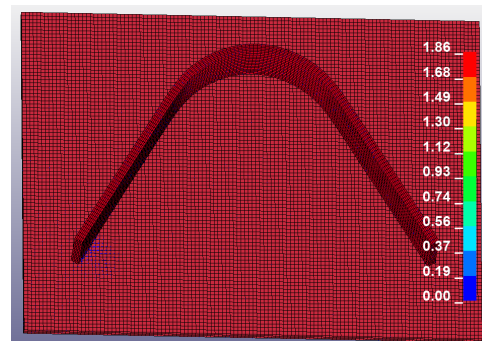
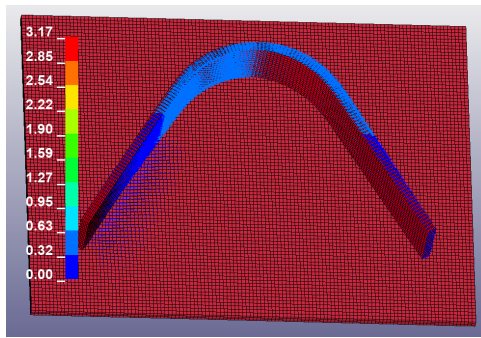
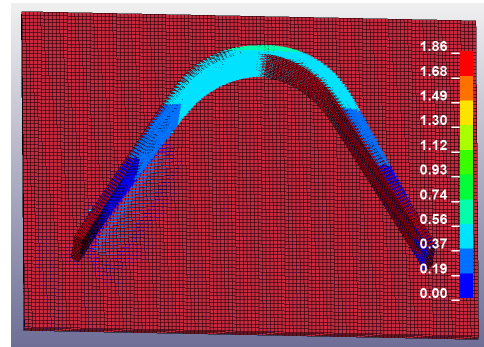


Figure 4.43: Vector displacement for Case A2 0.2 seconds into the laser welding process.



**Figure 4.44:** Vector displacement for Case A1 1.0 second into the laser welding process.



**Figure 4.45:** Vector displacement for Case A2 1.0 second into the laser welding process.

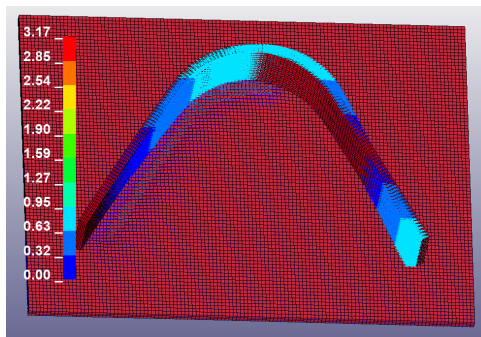


**Figure 4.46:** Vector displacement for Case A1 2.0 seconds into the laser welding process.

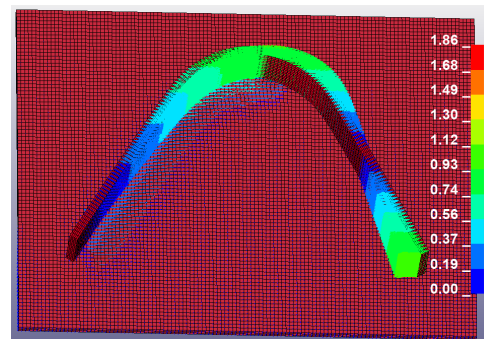


**Figure 4.47:** Vector displacement for Case A2 2.0 seconds into the laser welding process.

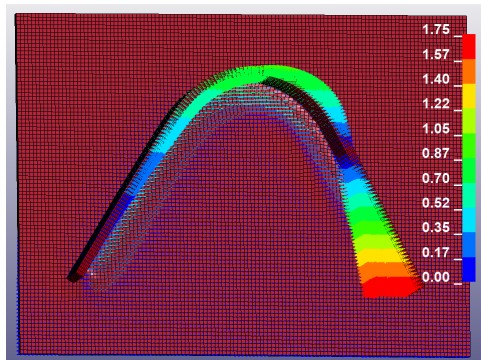


**Figure 4.48:** Vector displacement for Case A1 3.0 seconds into the laser welding process.

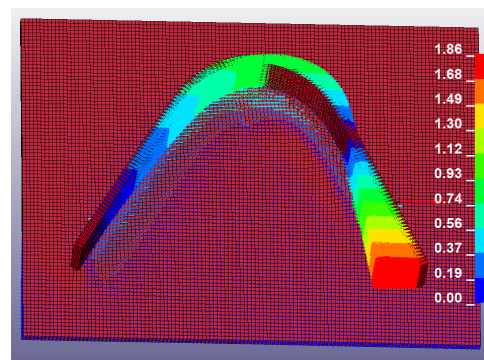


**Figure 4.49:** Vector displacement for Case A2 3.0 seconds into the laser welding process.

At initiation of the welding process there are almost no displacement in the bent plate in either cases. This changes during the process and both cases are experiencing large distortion in the bent plate. In this model, as with the others, the bent plate is moving inwards as the laser beam is approaching the bent area of the plate.

The distance between the edges of the bent plate for Case B1 and B2, post welding, are shown in figure 4.50 and 4.51, respectively. Having an initial distance

as the same as in Case A1 and A2, the distortion in Case B1 are calculated to 1.721 mm. The bent plate in Case B2 are mores distorted with a magnitude of 1.769 mm.

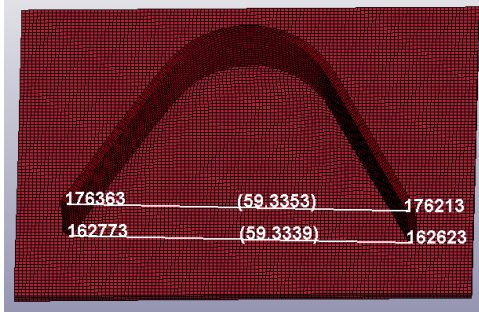


**Figure 4.50:** Distance between nodes at the edges of the bent plate after welding in Case A1.

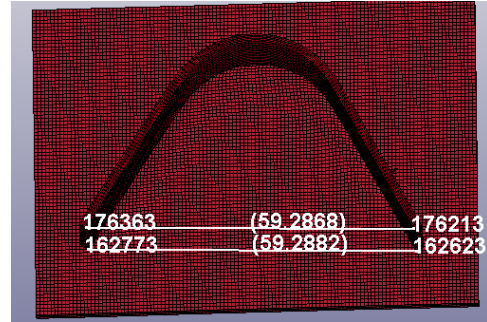


**Figure 4.51:** Distance between nodes at the edges of the bent plate after welding in Case A2.

### 4.3 Element distortion

From figure 4.52 it can be seen that the elements along the path of the laser beam get distorted due to exposure of high temperature gradients. This is an indication that the element size in the finite element model is not adequately small and should be reduced.

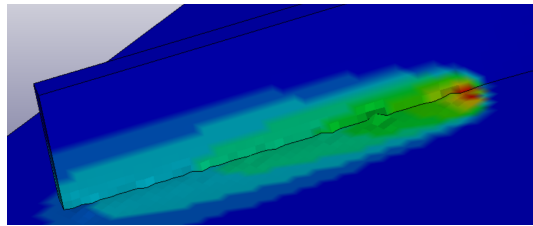


**Figure 4.52**

### 4.4 Summary

A summary of the distortions of the different models are given in table 4.1

Model	Case	Distortion
<b>Goldak Heat source</b>	Case A1	0.641 mm
	Case A2	0.745 mm
	Case B1	0.0005 mm
	Case B2	0.172 mm
<b>Conic Heat Source</b>	Case A1	1.721 mm
	Case A2	1.769 mm

**Table 4.1:** Distortion in the different models.

From this table it can be seen that the distortion seems to be larger in the models without no initial stresses. The difference between Goldak heat source Case A1 and A2, as well as Conic heat source model A1 and A2, is relatively small. The difference in distortion between the Goldak heat source Case B1 and B2 is of greater magnitude.

Between the models, the conical heat source have by far the largest displacement in the bent plate. This is likely due to the very high temperature gradients in the model during the laser welding process. Further it can seem that the distortions are less if the plate are welded from the outside compared to the inside.

## 4.5 Gap Closing

The figure 4.53 shows a cross section of the model where the laser beam is first approaching and then moving past the area. As can be seen, there is an initial gap between the parts that is closed in the laser welding process.

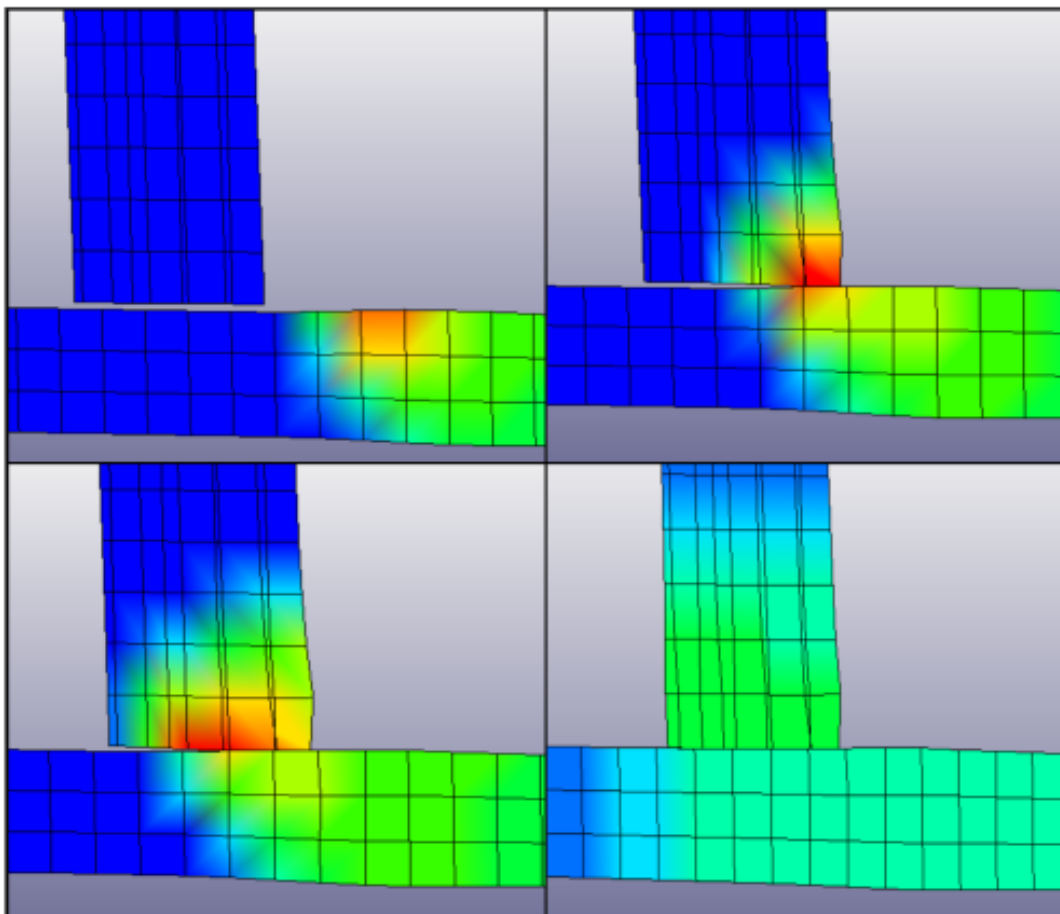


Figure 4.53: Closing of the initial gap between the parts during the welding.

## 4.6 Validation

The temperature fields of the finite element models will be compared to the analysis where the laser welding parameters were obtained.

The first set of weld parameters discussed are the for the Goldak heat source from [3]. The temperature was reported to be higher for the simulation than the experimental results. It was discussed that this could be due to inexact placing of the thermocouples measuring the temperature in the experiments or due to power efficiency. Lowering the power efficiency for the simulation the results show agreement with the experiments. The heat source parameters were also close to the weld pool dimensions of the weld experiment. The temperature in the weld pool is not presented for this study, but as the thickness of the material, material properties, convection, radiation and laser weld parameters are identical to the model reported in this study, it is assumed that the temperature field is similar. However, the power efficiency was neglected which will result in higher temperature gradients.

The second set of laser welding parameters were from [40], where the result was a temperature of about 2500 degrees Celsius at the top of the weld pool. Implementing these welding parameters in the finite element model the temperature gradients were much larger. One reason for the huge difference in temperature in the models could be the choice employing different a different volumetric heat source, as it decides how the heat is distributed in the work piece. Convection and radiation boundary conditions could also be important in the explanation of the different temperature fields.



# CONCLUSION

A three dimensional finite element model was presented for the simulation of laser welding on a thin sheet stainless steel structure. The numerical model used transient and thermal conductivity for calculation of the temperature field. For this purpose both a conical and double ellipsoidal heat source were employed in separate analysis. The model was intended to be validated by comparison of previous researchers work. The temperature field was compared and the laser welding parameters need some calibration.

The conclusion that can be drawn according to the result of the study:

- Initial stresses had very little effect on distortion in, if anything they seem to make the structure less distorted.
- Welding from the outside of the bent plate gave less distortion than from the inside.

## 5.1 Further work

As mentioned in section 3.6.2 the intention when starting this study was to also have a model with a denser mesh. This would be of interest as the elements where the heat input is highest in the finite element model gets distorted and the the temperature field is not constant throughout the model. The latter could also be due to the time step, but as the element size is rather large it is more likely that this is at fault.

The model should be validated against another set of welding parameters or calibrated against the ones already used. The first set of welding parameters were hard to validate against as the temperature field was not reported. The second set gave a huge difference in the temperature between the two model.



# BIBLIOGRAPHY

- [1] G. A. Moraitis and G. N. Labeas. "Residual stress and distortion calculation of laser beam welding for aluminum lap joints". In: (July 2007).
- [2] K. Manonmani, N. Murugan, and G. Buvanasekaran. "Effects of process parameters on the bead geometry of laser beam butt welded stainless steel sheets". In: (Apr. 2006).
- [3] K. Stampe A. F. Mikkelsen C. M. Farley and M. M Kristensen. "Simulation of laser beam welding process by applying a double-ellipsoid heat flux distribution". In: (May 2017).
- [4] M. Dal and R. Fabbro. "An overview of the state of art in laser welding simulation". In: (Sept. 2015).
- [5] Xiacong He. "Finite Element Analysis of Laser Welding: A State of Art Review". In: (July 2012).
- [6] Q. Pan P. Wang X. Chen and B. Madigan. "Laser welding dissimilar materials of aluminum to steel: an overview". In: (Apr. 2016).
- [7] Claus Thomy Won-Ik Cho Suck-Joo Na and Frank Vollertsen. "Numerical simulation of molten pool dynamics in high power disk laser welding". In: (Sept. 2011).
- [8] Holger Koch Andreas Otto and Rodrigo Gomez Vazquez. "Multiphysical Simulation of Laser Material Processing". In: (Oct. 2012).
- [9] Andreas Otto and Michael Schmidt. "Towards a universal numerical simulation model for laser material processing". In: (Aug. 2018).
- [10] Holger M. Koch Rodrigo Gómez Vázquez and Andreas Otto. "Multi-physical Simulation of Laser Welding". In: (Aug. 2014).
- [11] Marcel Bachmann Antoni Artinov and Michael Rethmeier. "Equivalent heat source approach in a 3D transient heat transfer simulation of full-penetration high power laser beam welding of thick metal plates". In: (Feb. 2018).
- [12] P. L. Masson M. Courtois M. Carin and Sadok Gaiied. "Guidelines in the experimental validation of a 3D heat and fluid flow model of keyhole laser welding". In: (Mar. 2016).
- [13] J. Mazumder H. Ki and P. S. Mohanty. "Modeling of laser keyhole welding: Part II. simulation of keyhole evolution, velocity, temperature profile, and experimental verification". In: (June 2002).

- [14] Y. Lei R. Wang and Y. Shi. "Numerical simulation of transient temperature field during laser keyhole welding of 304 stainless steel sheet". In: (Oct. 2010).
- [15] E. Cicala I. Bendaoud S. Matteï and I. Tomashchuk. "The numerical simulation of heat transfer during a hybrid laser-MIG welding using equivalent heat source approach". In: (Sept. 2013).
- [16] G. Basileb R. Spina L. Tricarico and T. Sibillano. "Thermo-mechanical modeling of laser welding of AA5083 sheets". In: (Mar. 2007).
- [17] Z. Jian H.GuoMing and L. JianQang. "Numerical simulation of molten pool dynamics in high power disk laser welding". In: (June 2006).
- [18] Jiamin Sun et al. "A comparative study on welding temperature fields, residual stress distributions and deformations induced by laser beam welding and CO<sub>2</sub> gas arc welding". In: (June 2014).
- [19] Muhammad Zain-ul-abdein et al. "Experimental investigation and finite element simulation of laser beam welding induced residual stresses and distortions in thin sheets of AA 6056-T4". In: (Jan. 2010).
- [20] M. R. Nami M. Asle Zaeem and M. H. Kadivar. "Prediction of welding buckling distortion in a thin wall aluminum T joint". In: (Mar. 2006).
- [21] M. Kraska T. Schenk I. M. Richardson and S. Ohnimus. "A study on the influence of clamping on welding distortion". In: (Jan. 2009).
- [22] J. F. Jullien M. Zain-ul-abdein D. Nélias and F. Boitout. "Finite element analysis of metallurgical phase transformations in AA 6056-T4 and their effects upon the residual stress and distortion states of a laser welded T-join". In: ( ).
- [23] K.Sankaranarayananasamy N. Siva Shanmugama G.Buvanashakaranb and S.Ramesh Kumarc. "A transient finite element simulation of the temperature and bead profiles of T-joint laser welds". In: (Apr. 2010).
- [24] Dean Deng and Hidekazu Murakawa. "Numerical simulation of temperature field and residual stress in multi-pass welds in stainless steel pipe and comparison with experimental measurements". In: (July 2005).
- [25] Dean Deng and Shoichi Kiyoshima. "Numerical simulation of residual stresses induced by laser beam welding in a SUS316 stainless steel pipe with considering initial residual stress influences". In: (Dec. 2009).
- [26] LIVERMORE SOFTWARE TECHNOLOGY CORPORATION (LSTC). *LS-DYNA® KEYWORD USER'S MANUAL, VOLUME I*. English. Version R11.
- [27] Amit Trivedi et al. "Modeling of Welding Heat Source for Laser Spot Welding Process". In: (May 2011).
- [28] Y. Lin C. Chen and H. Ou. "Study of Heat Source Calibration and Modelling for Laser Welding Process". In: (Aug. 2018).
- [29] Paulo Teixeira, Douglas Araújo, and Luiz Cunha. "Study of the gaussian distribution heat source model applied to numerical thermal simulations of TIG welding processes". In: *Ciencia and Engenharia/ Science and Engineering Journal* 23 (Dec. 2014), pp. 115–122. doi: 10.14393/19834071.2014.26140.

- [30] Aditya Chakravarty John Goldak and Malcolm Bibby. "A New Finite Element Model for Welding Heat Sources". In: (Feb. 1983).
- [31] H. G. Wang C. S. Wu and Y. M. Zhang. "A New Heat Source Model for Keyhole Plasma Arc Welding in FEM Analysis of the Temperature Profile". In: (Dec. 2006).
- [32] J. Bradáč and Mladá Boleslav. "CALIBRATION OF HEAT SOURCE MODEL IN NUMERICAL SIMULATIONS OF FUSION WELDING". In: (Nov. 2013).
- [33] K. R Balasubramnian et al. "Numerical and experimental investigation of laser beam welding of AISI 304 Stainless steel sheet". In: (2008).
- [34] A. G. Olabi K. Y. Benyounis and M. S. J. Hashmi. In: (Mar. 2007).
- [35] A. P. Tadamalle, Y. P. Reddy, and E. Ramjee. "Influence of laser welding process parameters on weld pool geometry and duty cycle". In: (Mar. 2013).
- [36] Jeng-Ywan Jeng, Tzuoh-Fei Mau, and Shyeu-Ming Leu. "Prediction of laser butt joint welding parameters using back propagation and learning vector quantization networks". In: (Feb. 2000).
- [37] W. J. Suder W. A. Ayoola and S. W. Williams. "Parameters controlling weld bead profile in conduction laser welding". In: (20).
- [38] K.Y. Benyounis, A.G. Olabi, and M.S.J. Hashm. "Effect of laser welding parameters on the heat input and weld-bead profile". In: (Feb. 2005).
- [39] Y. Gu et al. "Determination of parameters of double-ellipsoidal heat source model based on optimization method". In: (June 1984).
- [40] M. Nagy and M. Behulova. "Design of welding parameters for laser welding of thin-walled stainless steel tubes using numerical simulation". In: *IOP Conference Series: Materials Science and Engineering* 266 (Nov. 2017), p. 012013. DOI: 10.1088/1757-899X/266/1/012013.
- [41] Z. Jian H. GuoMing and L. JianQang. "Dynamic simulation of the temperature field of stainless steel laser welding". In: (June 2005).
- [42] Yunus A. Cenge and Afshin J. Ghajar. *Heat and Mass Transfer: Fundamentals Applications, 5th edition*. McGraw-Hill, 2015.
- [43] The Editors of Encyclopaedia Britannica. "Stefan-Boltzmann law". In: (June 2019).
- [44] *Convective heat transfer coefficients chart*. URL: [https://www.engineersedge.com/heat\\_transfer/convective\\_heat\\_transfer\\_coefficients\\_\\_13378.htm](https://www.engineersedge.com/heat_transfer/convective_heat_transfer_coefficients__13378.htm).
- [45] Mikron. *TABLE OF EMISSIVITY OF VARIOUS SURFACES*. [http://www-eng.lbl.gov/~dw/projects/DW4229\\_LHC\\_detector\\_analysis/calculations/emissivity2.pdf](http://www-eng.lbl.gov/~dw/projects/DW4229_LHC_detector_analysis/calculations/emissivity2.pdf). 20.
- [46] Matweb. *304 stainless steel*. URL: <http://www.matweb.com/search/DataSheet.aspx?MatGUID=abc4415b0f8b490387e3c922237098da&ckck=1>.

- [47] Dean Deng and Hidekazu Murakawa. "Numerical simulation of temperature field and residual stress in multi-pass welds in stainless steel pipe and comparison with experimental measurements". In: (July 2005).
- [48] LIVERMORE SOFTWARE TECHNOLOGY CORPORATION (LSTC). *LS-DYNA® KEYWORD USER'S MANUAL, VOLUME 2*. English. Version R11.
- [49] Dynamore. *Review of Solid Element Formulation in LS DYNA*. <https://www.dynamore.de/de/download/papers/forum11/entwicklerforum-2011/erhart.pdf>. Oct. 2011.
- [50] L. Zhang, E. W. Reutzl, and P. Michaleris. "Finite element modeling discretization requirements for the laser forming process". In: (June 2004).
- [51] Dynasupport. *The Next Step*. URL: <https://www.dynasupport.com/tutorial/getting-started-with-ls-dyna/the-next-step>.
- [52] E. Stamper. "Calculating Solution Settings for a Transient Thermal Analysis". In: (Aug. 2017).

# KEYWORD DECK

The keyword deck used for the finite element model are presented here.

## A.1 Control keywords

By enabling hourglass control zero energy modes are avoided, seen in figure A.1

```
*CONTROL_HOURGLASS
$#   ihq      qh
      6      0.1
```

Figure A.1: Control hourglass

```
*CONTROL_SOLID
$#  esort  fmatrix  niptets  swlocl  psfail  t10jtol  icohed  tet13k
      0      2      4      1      0      0.0      0      0
$#  pm1    pm2     pm3     pm4     pm5     pm6     pm7     pm8     pm9     pm10
      0      0      0      0      0      0      0      0      0      0
```

Figure A.2

```
*CONTROL_THERMAL_SOLVER
$#  atype  ptype  solver  cgto1  gpt  eqheat  fwork  sbc
      1      2  31.00000E-4  8  1.0  1.0  0.0
$#  msglvl  maxitr  abstol  reltol  omega  unused  unused  tsf
      0  5001.0000E-101.00000E-6  1.0  unused  unused  1.0
$#  mxdmp  dtvf  varden
      0  0.0  0
```

Figure A.3

```
*CONTROL_TIMESTEP
$#  dtinit  tssfacc  isdo  tslimit  dt2ms  lctm  erode  mslst
      0.0  0.9  0  0.0-1.00000E-7  0  0  0
$#  dt2msf  dt2mslc  imsc1  unused  unused  rmsc1  unused  ihdo
      0.0  0  0  0.0  0
```

Figure A.4

```
*CONTROL_TERMINATION
$#  endtim   endcyc      dtmin   endeng   endmas   nosol
      20.0      0      0.0    0.01.000000E9      0
```

Figure A.5

```
*CONTROL_THERMAL_NONLINEAR
$#  refmax      tol      dcp      lumpbc      thlstl      nlthpr      phchpn
      401.00000E-4      0.5      0      0.0      0      0.0
```

Figure A.6

## A.2 Database

Figure A.7 shows the database keywords used in this model. They define the number of plot outputs from the simulation.

```
*DATABASE_BINARY_D3DUMP
$#  cycl      lcdt      beam      npltc      psetid
      0.005      0      0      0      0
*DATABASE_BINARY_D3PLOT
$#  dt      lcdt      beam      npltc      psetid
      0.05      0      0      0      0
$#  ioopt      rate      cutoff      window      type      pset
      0      0.0      0.0      0.0      0      0
*DATABASE_EXTENT_BINARY
$#  neiph      neips      maxint      strflg      sigflg      epsflg      rltflg      engflg
      23      23      3      1      1      1      1      1
$#  cmpflg      ieverp      beamip      dcomp      shge      stssz      n3thdt      ialemat
      1      0      0      1      1      1      2      1
$#  nintsld      pkp_sen      sclp      hydro      msscl      therm      intout      nodout
      1      0      1.0      0      2      0
$#  dttdt      resplt      neipb      quadr      cubic
      0      0      0      0      0
```

Figure A.7: Database.

## A.3 Implicit

This section present the keywords used for setting up the implicit finite element analysis. The first figure A.8 defines the parameters for automatic step size control.

```
*CONTROL_IMPLICIT_AUTO
$#  iauto      iteopt      itewin      dtmin      dtmax      dtexp      kfail      kcycle
      1      11      5      0.0      0.1      0.0      0      0
```

Figure A.8: Implicit auto

Figure A.9 is the keyword activating implicit mode and defines the implicit time step.

```
*CONTROL_IMPLICIT_GENERAL
$# imflag      dt0      imform      nsbs      igs      cnstn      form      zero_v
      1        0.1        2          1          1          0          0          0
```

Figure A.9: Implicit general.

The keyword defining the parameters for nonlinear equation solver and convergence solver can be seen in figure A.10.

```
*CONTROL_IMPLICIT_SOLUTION
$# nsolvr      ilimit      maxref      dctol      ectol      rctol      lstol      abstol
      2          11          15          0.001      0.01       0.01       0.91.0000E-10
$# dnorm      diverg      istif      nlprint      nlnorm      d3itctl      cpchk
      2          1          1          0          2          0          0
$# arcctl      arcdir      arclen      arcmtl      arcdmp      arcpsi      arcalf      arctim
      0          0          0.0        1          2          0          0          0
$# lsmtl      lsdir      irad      srad      awgt      sred
      4          2          0.0        0.0        0.0        0.0
```

Figure A.10: Implicit solution.

Figure A.11 is the keyword used to output the calculations from the finite element analysis.

```
*CONTROL_IMPLICIT_SOLVER
$# lsolvr      lprint      negev      order      drcm      drcprm      autospc      autotol
      2          1          2          0          4          100.0       11.10000E-7
$# lcpack      mtxdmp      iparm1      rparm1      rparm2
      2          0          500        0.0        0.001
$# emxdmp      rdcmem
      0          0.85
```

Figure A.11: Implicit solver.

## A.4 Boundary Conditions

Figure A.12 and A.13 are the thermal boundary conditions, applying convection and radiation to the model.

```
*BOUNDARY_CONVECTION_SET
$#      ssid      pserod
      2          0
$#      hlcid      hmult      tlcid      tmult      loc
      0          0.1        0          293.0      0
```

Figure A.12: Heat transfer by convection.

```

*BOUNDARY_RADIATION_SET
$#  ssid      type
    1         1         0         0         0         0         0
$#  rflcid    rfmult    tilcid    timult    loc
    04.5360E-11    0         293.0         0

```

Figure A.13: Heat transfer by radiation.

Figure A.14 set the initial temperature of the model to the ambient temperature of 293 K.

```

*INITIAL_TEMPERATURE_SET
$  NSID      TEMP      LOC
$#  nsid     temp     loc
    2        293.0     0

```

Figure A.14: Initial temperature of the model.

## A.5 Parts and Material

Figure A.15 and A.16 shows the PART keyword for the bent plate and stiffener in the model. It defines the part ID, sections, as well as the mechanical and thermal material ID's.

```

*PART
$#                                     title
Stiffener
$#  pid    secid    mid    eosid    hgid    grav    adpopt    tmid
    1      1      20      0      0      0      0      21
*PART
$#                                     title
Bent plate
$#  pid    secid    mid    eosid    hgid    grav    adpopt    tmid
    11     11     20      0      0      0      0      21

```

Figure A.15: The parts of the model

```

*SECTION_SOLID_TITLE
Stiffener solid
$#  secid    elform    aet
    1        2         0
*SECTION_SOLID_TITLE
Bent plate solid
$#  secid    elform    aet
    11       2         0

```

Figure A.16: Sections

Figure A.17 and A.18 is the keywords for the mechanical and thermal material model.

```

*MAT_CWM_TITLE
$#   mid      ro      lcm      lcpr      lcsy      lchr      lcat      beta
      207.90000E-9      11      12      13      14      15      0.0
$#  tastart  taend  tlstart  tlend  eghost  pghost  aghost
      1331.0  1773.0-1.00000E8 -1000000  10000.0  0.2841.0000E-20
$#  t2phase  tlphase
      0.0      0.0

```

Figure A.17: Mechanical material properties for the model

```

*MAT_THERMAL_CWM_TITLE
$#   tmid      tro      tgrlc      tgmult      hdead      tdead      tlat      hlat
      21      0.0      0.0      0.0      0.0      0.0      0.0      0.0
$#   lchc      lctc      tlstart      tlend      tistart      tiend      hghost      tghost
      211      212      -1000.0      -1000.0      0.0      0.06.500000E8  0.001

```

Figure A.18: Thermal material properties for the model.

## A.6 contact

Figure A.19 is the keyword defining the contact between the two parts of the model.

```

*CONTACT_AUTOMATIC_SURFACE_TO_SURFACE_TIED_WELD_THERMAL
$#   cid      title
$#   ssid      msid      sstyp      mstyp      sboxid      mboxid      spr      mpr
      11      1      3      2      0      0      0      0
$#   fs      fd      dc      vc      vdc      penchk      bt      dt
      0.1      0.0      0.0      0.0      0.0      0      0.01.00000E20
$#   sfs      sfm      sst      mst      sfst      sfmt      fsf      vsf
      1.0      1.0      0.0      0.0      1.0      1.0      1.0      1.0
$#   temp      close      hclose      ntpm      nmhis
      1773.0      0.2      14.0      0      0
$#   cf      frad      htc      lmin      lmax      ftoslv      bc_flg      algo
      14.04.5360E-11      0.0      0.1      1.0      0.5      0      0
$#   soft      sofsc1      lcidab      maxpar      sbopt      depth      bsort      frcfrq
      0      0.1      0      1.025      2.0      2      0      1
$#   penmax      thkopt      shlthk      snlog      isym      i2d3d      sldthk      sldstf
      0.0      0      0      0      0      0      0.0      0.0
$#   igap      ignore      dprfac      dtstif      unused      unused      flangl      cid_rcf
      3      0      0.0      0.0      unused      unused      0.0      0

```

Figure A.19